Cancer Cell International

RESEARCH

Open Access

Spatial transcriptomics and single-cell analyses reveal the role of the cisplatin-resistant gene panel in NSCLC progression and the tumor microenvironment, identifying LOXL2 as a potential therapeutic target

Junzhi Liu[1†], Huimin Li[2†], Yuheng Jiao[3†] and Meng Hou[1*]

Abstract

Background Non-small cell lung cancer (NSCLC) patients often develop resistance to platinum-based chemotherapy, especially cisplatin, leading to treatment failure. This study aimed to identify high-score epithelial cells in tumors within the cisplatin-resistant gene panel (CRGP) and investigate their role in tumor progression and the microenvironment.

Methods Using cisplatin-resistant cell datasets from GEO and TCGA for NSCLC, we identified the CRGP and its clinical significance. By integrating five single-cell datasets and applying 13 scoring methods, we identified tumor epithelial cells with high CRGP scores (CRGPhighepi). We evaluated drug sensitivity using the BeyondCell algorithm and studied intrinsic mechanisms using Cytotrace, Monocle, SCENIC, and CellCall. Spatial transcriptomics and deconvolution methods identified CRGPhighepi and other cell types. The prognostic model, designated as SuperPCCRGP, was constructed. Subsequent CRGP co-expression network analysis revealed an association between CRGP and LOXL2, implicating their roles in cisplatin resistance. The impact of LOXL2 on cisplatin sensitivity was further validated through *in vitro* experiments.

Results CRGP was identified as a potential risk factor for NSCLC prognosis. High CRGP score epithelial cells (CRGPhighepi) activate pathways related to cell cycle and DNA repair and interact with smooth muscle cells. CRGPhighepi exhibits drug resistance to Cisplatin and Paclitaxel. The SuperPC model showed robust predictive performance. LOXL2 was linked to poor prognosis and therapy response. LOXL2 knockdown enhanced cisplatin sensitivity in NSCLC.

Keywords Smooth muscle cell, Spatial transcriptomics, Single-cell RNA sequencing, LOXL2, Therapeutic target, Biomarker

†Junzhi Liu, Huimin Li and Yuheng Jiao contributed equally.

*Correspondence:
Meng Hou
houmengdr@163.com

[1]Department of Oncology, Shanghai Pulmonary Hospital, School of Medicine, Tongji University, Shanghai 200433, China
[2]Internal Medicine Residency Training Base, Gongli Hospital of Shanghai Pudong New Area, Shanghai 200135, China
[3]Department of Heart failure, Shanghai East Hospital, School of Medicine, Tongji University, Shanghai 200120, China

Introduction

Non-small cell lung cancer (NSCLC) is the most common histological type of lung cancer, and cisplatin resistance is frequently observed in NSCLC patients, severely affecting chemotherapy efficacy and patient prognosis [1, 2]. Single-cell technology allows for in-depth study of the biological characteristics of NSCLC at the single-cell level, helping to uncover the mechanisms of cisplatin resistance. Various genes and signaling pathways have been found to be associated with cisplatin resistance in NSCLC at the single-cell level. For example, EDN1 is upregulated in cisplatin-resistant NSCLC cells and promotes cell proliferation, invasion, migration, and inflammatory responses by regulating the TNF signaling pathway, thereby enhancing cisplatin resistance. Inhibition of EDN1 can reverse this phenomenon [3]. Heme oxygenase 1 (HO-1), a key resistance gene downstream of Nrf2, induces ferroptosis resistance and leads to cisplatin resistance. Compounds such as SB 202,190 and Nordihydroguaiaretic acid (NDGA) can reactivate ferroptosis by inhibiting HO-1, increasing cisplatin sensitivity [4]. Additionally, Kinase Suppressor of Ras 1 (KSR1) plays a crucial role in tumor initiation and cisplatin resistance in small cell lung cancer (SCLC). CRISPR/Cas9-mediated KSR1 knockout prevents SCLC cells from developing cisplatin resistance [5]. Furthermore, spatial transcriptomics has identified certain cell states and intercellular interactions associated with drug resistance in various cancer types. For instance, in melanoma meningitis, tumor-stroma interactions activate tumor-promoting signaling pathways, leading to reduced sensitivity to MAPK inhibitors. Blocking these pathways can resensitize the tumor cells [6]. In endometrial cancer, blocking netrin-1 suppresses tumor growth and epithelial-mesenchymal transition (EMT) characteristics. Spatial transcriptomic analysis of pre- and post-treatment biopsy samples revealed changes in immune infiltration and intercellular interactions within the tumor microenvironment, influencing cisplatin resistance [7].

Cisplatin primarily exerts its cytotoxic effect by forming platinum-DNA adducts, inducing DNA damage, and triggering apoptosis. However, tumor cells can counteract cisplatin-induced damage through various DNA damage repair mechanisms, leading to resistance. For example, in NSCLC, the expression of XPF (xeroderma pigmentosum group F complementing protein) mRNA is closely related to cisplatin resistance. In cisplatin-resistant NSCLC cell lines, XPF expression is upregulated, and silencing XPF significantly restores cisplatin sensitivity [8]. Moreover, USP22 enhances DNA damage repair by promoting phosphorylation of histone H2AX and stabilizing Sirt1 to reduce the acetylation of Ku70, inhibiting Bax-mediated apoptosis, and thereby inducing cisplatin resistance in NSCLC cells [9]. RIF1 regulates the MYC signaling pathway, affecting the expression of genes involved in the cell cycle and DNA double-strand break repair, thus influencing NSCLC patients' response to platinum-based chemotherapy. Patients with high RIF1 expression have a shorter survival time [10]. Aberrant cell cycle regulation plays a crucial role in NSCLC cisplatin resistance. Studies have shown that the cisplatin-resistant NSCLC cell line A549rCDDP2000 lacks cisplatin-induced G2/M cell cycle arrest. Compared to cisplatin-sensitive A549 cells, apoptosis is reduced despite similar levels of platinum-DNA adducts [11]. This suggests that changes in cell cycle regulation may lead to resistance to cisplatin-induced apoptosis. Several genes and signaling pathways are involved in the process of cell cycle alterations and cisplatin resistance. For example, BCAT1 promotes cell proliferation and induces the S-G2/M phase transition in liver cancer cells, leading to chemotherapy resistance to cisplatin. Its transcription is regulated by MYC [12]. miR-223 regulates the G1/S transition of the cell cycle by targeting FBXW7 in gastric cancer cells, affecting cisplatin resistance. Upregulation of miR-223 expression leads to cisplatin resistance [13]. These studies suggest that regulating cell cycle-related genes and signaling pathways may restore cisplatin sensitivity in resistant cells.

To overcome cisplatin resistance in NSCLC, combination therapy has become a research focus. Several drugs, when combined with cisplatin, have shown synergistic effects. For instance, panobinostat, a histone deacetylase (HDAC) inhibitor, reduces hypoxia-induced cisplatin resistance in NSCLC cells. This occurs through the destabilization of HIF-1α and HDAC4, enhancing cisplatin-induced apoptosis [14]. Targeted therapies focusing on specific molecular targets related to cisplatin resistance in NSCLC offer new avenues for overcoming resistance. Studies have found that certain genes and signaling pathways play critical roles in NSCLC cisplatin resistance, and targeting these pathways may improve treatment efficacy. For example, MCL-1, an important anti-apoptotic member of the Bcl-2 family, plays a significant role in cisplatin resistance in NSCLC cells. Obatoclax, by inhibiting MCL-1, restores the function of NOXA and BAK, promoting mitochondrial apoptosis and reversing cisplatin resistance [15]. In NSCLC, inhibiting the PI3K/Akt/mTOR signaling pathway can overcome cisplatin resistance. For instance, NVP-BEZ235 combined with cisplatin shows synergistic effects in cisplatin-resistant triple-negative breast cancer cell line HCC38, restoring cisplatin sensitivity [16]. These targeted therapeutic strategies offer more personalized treatment options for NSCLC patients with cisplatin resistance.

This study aimed to identify a cisplatin-resistant gene panel (CRGP), its clinical relevance, and pathway correlations. By integrating multiple single-cell datasets and applying various scoring methods, tumor epithelial cells

with high CRGP scores (CRGPhighepi) were identified. The intrinsic mechanisms and developmental trajectories of CRGPhighepi were explored through transcription factor analysis, pseudotime analysis, and RCTD deconvolution of spatial transcriptomics. Using cell communication analysis and mistyR, the interactions between CRGPhighepi and smooth muscle cells and their potential dependence on cell cycle and DNA damage repair pathways were explored. Based on CRGP, we developed a prognostic model (SuperPCCRGP) and identified potential therapeutic strategies for targeting the high CRGP score group. Laboratory experiments suggested that lysyl oxidase homolog 2 (LOXL2) may be involved in NSCLC cell cycle, proliferation, and DNA damage repair processes. Inhibition of LOXL2 potentially enhanced the sensitivity of NSCLC epithelial cells to cisplatin. However, it should be noted that this study only includes certain *in vitro* experiments, and further validation through rescue experiments and in vivo animal studies is necessary. These findings contribute to our understanding of cisplatin resistance mechanisms and offer potential new targets for overcoming resistance in NSCLC.

Methods and materials

Data acquisition

The single-cell RNA sequencing dataset EMTAB6149 and the spatial transcriptomics dataset EMTAB13530 were obtained from the ArrayExpress database (https://www.ebi.ac.uk/biostudies/arrayexpress). Additional single-cell RNA-seq datasets, including GSE6410, GSE21656, GSE127465, GSE131907, GSE149655, and GSE153935, as well as bulk transcriptomic datasets GSE11969, GSE12428, GSE31210, GSE41271, GSE42127, GSE72094, GSE31547, GSE40791, GSE21933, and GSE33479, were retrieved from the GEO database (https://www.ncbi.nlm.nih.gov/geo/). Bulk transcriptomic profiles of TCGA-NSCLC samples, along with corresponding clinical information, were downloaded from the UCSC Xena platform (https://xena.ucsc.edu/). Proteomic data from the CPTAC cohort were obtained from https://pdc.cancer.gov. Gene sets representing 12 tumor-related pathways or functional states were retrieved from the CancerSEA database (http://biocc.hrbmu.edu.cn/CancerSEA/), while Reactome, Hallmark, and KEGG-related gene sets were sourced from the Molecular Signatures Database (MSigDB; https://www.gsea-msigdb.org/gsea/msigdb/). Mendelian randomization analyses were conducted using the TwoSampleMR R package by leveraging lung cancer GWAS summary statistics. Drug sensitivity data for bulk transcriptomic analyses were obtained from the Cancer Therapeutics Response Portal (CTRP v2.0, released in October 2015; https://portals.broadinstitute.org/ctrp) and the PRISM Repurposing dataset (version 19Q4, released in December 2019; https://depmap.org/portal/prism/). Immunotherapy response prediction based on bulk transcriptomic profiles was conducted using the TIDE (Tumor Immune Dysfunction and Exclusion) framework (http://tide.dfci.harvard.edu/).

Single-Cell RNA-seq quality control and downstream analyses

The single-cell RNA sequencing data were comprehensively processed using the Seurat R package [17]. Initial quality control steps involved: (a) removing genes detected in fewer than three cells; (b) excluding cells expressing fewer than 50 genes; and (c) filtering out cells with ≥ 5% mitochondrial gene expression. Normalization was performed using the SCTransform method, and batch effects across five single-cell RNA-seq datasets (EMTAB6149, GSE127465, GSE131907, GSE149655, and GSE153935) were corrected using the harmony algorithm [18]. Marker genes for each cell cluster were identified with the FindMarkers function, and cell-type annotation was conducted by referencing the CellMarker database [19]. To evaluate functional states at the single-cell level, enrichment scores were computed using 13 distinct algorithms implemented in the irGSEA package [20]. Drug response predictions were performed using the beyondcell package [21], while stemness features were quantified using the CytoTRACE algorithm [22]. Pseudotemporal ordering of cells was reconstructed with the Monocle2 package [23–25]. Transcription factor activity was inferred using the SCENIC package, intercellular communication was analyzed via the CellCall framework [26], and metabolic pathway activity was estimated using the scFEA algorithm [27].

Spatial transcriptomics analyses

The spatial transcriptomics (ST) data were processed using the Seurat R package, with cell-type annotations inferred based on the integrated single-cell dataset using the RCTD algorithm [28]. Malignant regions within the spatial data were delineated using the Cottrazm algorithm [29]. To assess pathway activity across spatial contexts, the ssGSEA method from the irGSEA package [20] was employed. Spatial evolutionary trajectories were reconstructed using the stLearn algorithm [30], and both pathway and cell-type dependency relationships were analyzed with the misty framework [31].

Machine learning algorithms

A set of machine learning algorithms was applied to build an integrated survival prediction model. The methods included random survival forests (RSF), LASSO, elastic net (Enet), Stepwise Cox, supervised principal component analysis (SuperPC), CoxBoost, Ridge regression, survival support vector machines (survival SVM), partial least squares regression for Cox models (plsRcox),

and gradient boosting machine (GBM). Each algorithm was configured to identify the model with the highest concordance index (C-index) across validation datasets. The predictive performance of the resulting risk score was evaluated using the timeROC package by calculating the area under the curve (AUC). The risk score was confirmed to be an independent prognostic factor based on Cox regression analysis performed with the survival R package.

Weighted co-expression network analysis

We performed weighted gene co-expression network analysis (WGCNA [32]) on the GSE21656 dataset. Samples were first stratified into cisplatin-resistant and cisplatin-sensitive groups based on clinical annotations. Additionally, samples were divided into quartiles according to LOXL2 expression levels: the top 25% were designated as Q1, the top 50% as Q2, the top 75% as Q3, and the remainder as Q4. Co-expression modules associated with cisplatin resistance and LOXL2 expression phenotypes were identified, and their correlations were further examined. Protein-protein interaction (PPI) analysis for genes within key modules belonging to the Cisplatin-Resistant Gene Panel (CRGP) was conducted using the STRING database [33]. The resulting networks were visualized using Cytoscape v3.9.1 [34].

Cell culture and transient suppression of LOXL2 expression

H520 and PC9 cells were procured from the Cell Bank of the Chinese Academy of Sciences in Shanghai, China, and maintained in a meticulously controlled environment, ensuring a 5% CO_2 atmosphere at 37°C. These cells were cultured in RPMI 1640 medium (Boster, China) supplemented with 10% fetal bovine serum (FBS; HyClone, USA) to promote optimal growth conditions. Establishment of drug-resistant cell line: At 80–90% confluence, H520 cells were treated with low-dose cisplatin (1/10 IC50 of parental H520) for 24 h. After cell density dropped to 50%, the medium was discarded, cells were PBS-washed twice, and drug-free medium was added for recovery. This cycle (treatment to recovery) was repeated 6× at the same concentration. Upon stable growth, cisplatin concentration was doubled incrementally until final resistance was achieved. The IC50 of resistant cells was measured, and resistance index (RI) was calculated as: RI = IC50 (resistant)/IC50 (parental). An RI > 5 defined a resistant strain (see Supplementary Figure. 1 for IC50 and RI values). To achieve transient suppression of LOXL2 expression in both H520 and PC9 cells, specific small interfering RNAs (siRNAs) from GenePharma (Suzhou, China) were transfected into the cells using Lipofectamine 3000. The siRNA sequences employed to target LOXL2 included a negative control (NC) sequence (5'-GGGAACTTAAGTAACCTTTGTTTGA-3'), along with two specific LOXL2-targeting sequences: siRNA-LOXL2#1 (5'-GGGTTCAAATTTGACAATTCGTTGA-3') and siRNA-LOXL2#2 (5'-CACAGGCAATGAGAAGTCCATTATA-3'). This strategic approach allowed for a nuanced investigation into the role of LOXL2 in the cellular behavior of these lines.

Cell viability assay

Cells were digested and centrifuged, then seeded into 96-well plates at a density of 2,500 cells per well. Cell viability was measured at 24, 48, 72, and 96 h using the Cell Counting Kit-8 (APExBIO, USA) according to the manufacturer's instructions. For cisplatin treatment, a concentration gradient of 0, 2, 4, 6, 8, 10, and 12 μg/mL was applied. Viability data were collected to assess drug response over time.

Western blotting (WB)

Cells were lysed in ice-cold lysis buffer containing phosphatase and protease inhibitors. Protein concentration was determined using the BCA assay. Samples were separated via 4–12% SDS-PAGE and transferred to PVDF membranes. After blocking, membranes were incubated with primary antibodies and then secondary antibodies. Chemiluminescence was used for detection. Primary antibodies included: anti-LOXL2 (HUABIO, ER1803-41, 1:1000), anti-cyclinD1 (Santa, sc-8396, 1:1000), anti-cyclinE1 (Santa, sc-377100, 1:1000), anti-CDK4 (Santa, sc-23896, 1:1000), anti-P21 (Santa, sc-397, 1:1000), anti-GAPDH (Santa, sc-137179, 1:1000), and anti-beta-actin (Santa, sc-58673, 1:1000).

Evaluation of cell migration capabilities

Cell migration was assessed using Boyden chambers with 8-μm pore size. H520 and PC9 cells (1×10^5 in 200 μL serum-free medium) were seeded in the upper chamber (BD, USA), while the lower chamber contained medium with 20% FBS. After 24 h, migrated cells were fixed, stained, and counted in six random microscopic fields.

The 5-Ethynyl-2′-Deoxyuridine (EdU) assay

To evaluate proliferation, 5×10^4 transfected cells were plated in 24-well plates and incubated overnight at 37 °C. The EdU Cell Proliferation Kit with Alexa Fluor 594 (BeyoClick) was used per the manufacturer's protocol. Cells were stained with Azide 594 and Hoechst 33,342. Images were taken from three random fields. Proliferation rate was calculated as: EdU-positive cells/(EdU-positive + EdU-negative cells) × 100%.

Immunofluorescence staining

Cells were cultured on 18-mm coverslips and incubated overnight at 37 °C. Samples were blocked with 5% BSA, then incubated with primary and fluorescent

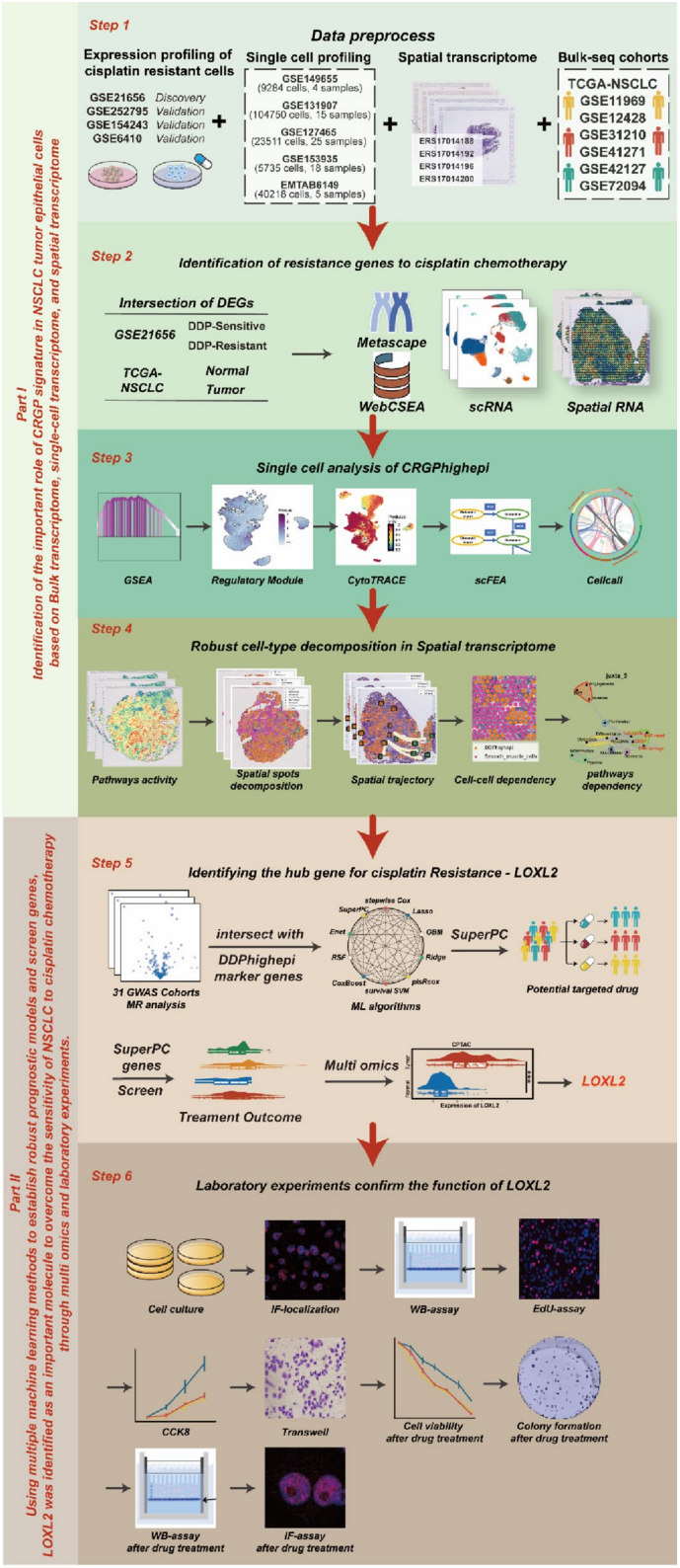

Fig. 1 The workflow of the study

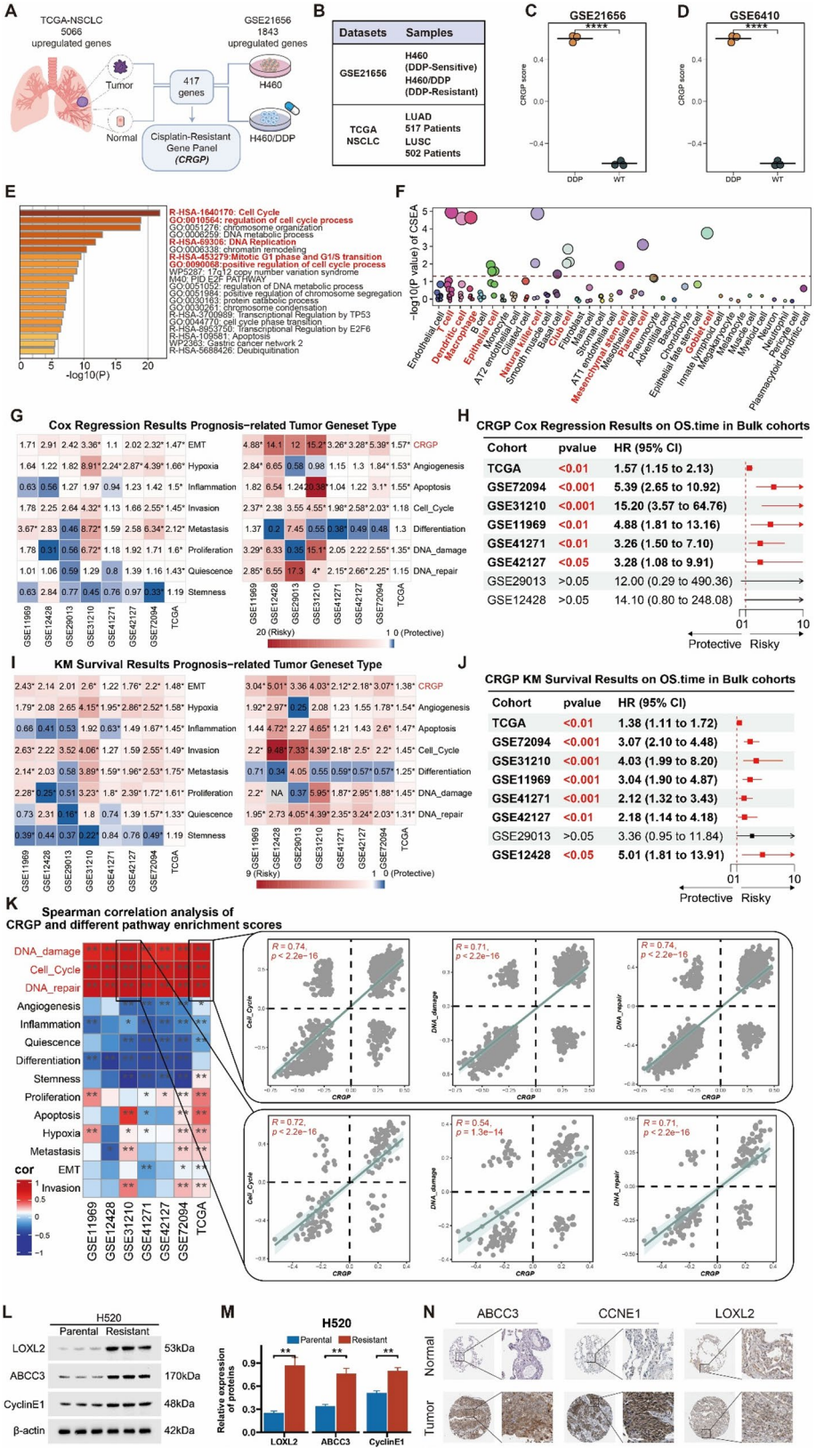

Fig. 2 (See legend on next page.)

(See figure on previous page.)

Fig. 2 Identification and function of the cisplatin-resistant gene panel (CRGP) in NSCLC. (**A**) Schematic diagram of the source of the CRGP in NSCLC. (**B**) Details of the data used for the gene panel. (**C**) The CRGP score is elevated in cisplatin-resistant cell lines in GSE21656. (**D**) The CRGP score is elevated in cisplatin-resistant cell lines in GSE6410. (**E**) Enrichment analysis of the CRGP. (**F**) Cell type distribution analysis of the CRGP. (**G**) Heatmap showing the Cox regression analysis of the prognostic value of CRGP and tumor-related pathways across the bulk cohorts. (**H**) Cox regression analysis of the prognostic value of the CRGP score across multiple bulk cohorts. (**I**) Heatmap showing the KM survival analysis of the prognostic value of CRGP and tumor-related pathways across the bulk cohorts. (**J**) Kaplan-Meier survival analysis of the CRGP score across multiple bulk cohorts. (**K**) Heatmap and scatterplot showing the correlation between the CRGP score and tumor-related pathways across multiple bulk cohorts. (**L**-**M**) The representative genes of the CRGP, LOXL2, ABCC3, and CCNE1, show increased protein expression in the H520-resistant cell line. (**N**) Immunohistochemical staining shows elevated expression of the representative CRGP genes LOXL2, ABCC3, and CCNE1 in tumor tissues. ****$P < 0.0001$, ***$P < 0.001$, **$P < 0.01$, *$P < 0.05$, ns $P > 0.05$

secondary antibodies. Nuclei were stained with DAPI (Thermo). Imaging was conducted using a Zeiss LSM 880 microscope. Primary antibodies included anti-LOXL2 (HUABIO, ER1803-41, 1:50) and anti-gamma-H2AX (HUABIO, ET1602-2, 1:100).

Colony formation assay

Approximately 8×10^2 to 1×10^3 cells were plated in 6-well plates and incubated for 10–14 days at 37 °C. Colonies were fixed with methanol for 15–30 min and stained with 1% crystal violet for 15 min. Colonies were then counted to assess proliferation capacity.

Statistical analysis

Data are presented as mean ± standard deviation. Categorical variable comparisons, including clinical subgroups, were assessed using the chi-squared test. A P-value < 0.05 was considered statistically significant. The Benjamini-Hochberg method was used to adjust P-values for multiple testing. All analyses were performed using R software.

Results

Identification of cisplatin-resistant gene panel (CRGP)

The workflow of this study is outlined in Fig. 1. We began by analyzing the TCGA-NSCLC and GSE21656 cohorts (Fig. 2A), with corresponding sample information presented in Fig. 2B. Differential analysis of the TCGA-NSCLC and GSE21656 datasets identified genes consistently upregulated in tumor tissues and cisplatin-resistant groups (Supplementary Table 1), leading to the identification of the cisplatin-resistant genomic panel (CRGP) (Supplementary Table 2). GSVA analysis of various GSE cohorts confirmed upregulation of CRGP in cisplatin-resistant cell groups (Fig. 2C-D). Enrichment analysis via the Metascape database revealed significant associations between the CRGP and key cell cycle-related pathways, including R-HSA-1,640,170, GO:0010564, R-HSA-453,279, and GO:0090068 (Fig. 2E), highlighting the panel's involvement in cellular replication and progression. Further exploration of cell and tissue specificity using the WebCESA database revealed that CRGP exhibits predominant expression across various lung-associated cell types, including T cells, dendritic cells, macrophages, epithelial cells, Clara cells, plasma cells, natural killer cells, goblet cells, and mesenchymal stem cells (Fig. 2F), indicating its role in both cell cycle regulation and immune responses within the lung microenvironment.

To assess the clinical relevance of CRGP, Cox regression and Kaplan-Meier survival analyses were performed across different NSCLC bulk cohorts. The analyses revealed that CRGP, along with pathways related to cell cycle, DNA damage repair, apoptosis, and hypoxia, were risk factors, whereas tumor stemness and differentiation pathways were protective factors (Fig. 2G-J). CRGP demonstrated stable prognostic value (HR > 1, $p < 0.05$), suggesting its potential as a prognostic biomarker for NSCLC. Pathway consistency analysis showed a significant positive correlation between CRGP and pathways associated with cell cycle and DNA damage repair ($R > 0.7$, $p < 0.05$), and a negative correlation with pathways such as angiogenesis, inflammation, quiescence, and differentiation (Fig. 2K). Additionally, we constructed cisplatin-resistant cell lines and performed IC50 testing (Supplementary Fig. 1). Representative CRGP genes, including LOXL2, ABCC3, and CCNE1, showed elevated protein expression in the H520 cisplatin-resistant cell line (Fig. 2L-M), with immunohistochemical staining further confirming stronger expression in tumor tissues (Fig. 2N). These findings underscore the critical role of CRGP in cisplatin resistance and its potential as a prognostic factor in NSCLC.

Elevated cisplatin-resistant gene panel in epithelial cells of NSCLC individuals

To investigate the cell specificity of CRGP, data from five single-cell NSCLC cohorts were integrated (Supplementary Fig. 2). After correcting for batch effects, dimensionality reduction, clustering, and cell annotation were conducted to ensure accurate downstream analysis (Fig. 3A). Using 13 distinct single-cell scoring methods, CRGP scores were evaluated across various cell populations, with average scores compared systematically (Fig. 3B-C). NSCLC epithelial cells exhibited the highest CRGP scores, highlighting their central role in cisplatin resistance. Further, the R package Cottrazm was used to differentiate malignant and benign regions within spatial transcriptomic data (Supplementary Fig. 3A-D). Spatial pathway scoring revealed significantly higher

CRGP scores in malignant tissues compared to benign ones (Fig. 3D-G). This spatially resolved analysis underscores CRGP enrichment in tumor regions, suggesting its involvement in malignancy and therapeutic resistance within the tumor microenvironment.

To explore potential differences in drug sensitivity associated with CRGP grouping, we applied the BeyondCell algorithm to analyze drug responses and related signaling pathways in CRGP-grouped cells (Supplementary Fig. 4 A). The results suggested that CRGPhighepi cells may be more sensitive to drugs such as PROSTAGLANDIN-A1 (sig-6785), SR-142,948 (sig-3284), and DC-45-A2 (sig-6173), while showing lower sensitivity to compounds like KU-C103881 (sig-980) (Supplementary Fig. 4B). Additionally, CRGPhighepi cells appeared less responsive to Cisplatin and Paclitaxel (Supplementary Fig. 4C-E), which may reflect a degree of resistance to these agents. These observations are in line with the rationale for CRGP-based stratification and may reflect characteristics associated with the CRGP score. Furthermore, CRGPhighepi cells showed relatively higher sensitivity to CDK1-5 inhibitors and Su-11,274 (Supplementary Fig. 4F-H), both of which are known to affect cell cycle processes, implying that cell cycle-related pathways might be relevant in this context. Similarly, sensitivity to Fenretinide and Trapidil was observed (Supplementary Fig. 4I-K). Regarding drug response-related signaling pathways (Supplementary Fig. 5 A), CRGPhighepi cells exhibited elevated activity in several pathways related to the cell cycle and DNA regulation, such as sig_G1S_WHITFIELD (Supplementary Fig. 5B-C), sig_cell_cycle_CancerSEA (Supplementary Fig. 5D-E), sig_proliferation_CancerSEA (Supplementary Fig. 5F-G), and sig_DNA_damage_CancerSEA (Supplementary Fig. 5H-I). These findings align with previous observations that CRGP is associated with cell proliferation and DNA repair processes. To further examine the spatial dimension of CRGP-associated drug sensitivity, we projected CRGP groups onto spatial transcriptomics data using a deconvolution algorithm (Supplementary Fig. 6A-C). Drug response analyses across spatial transcriptomic samples suggested that CRGPhighepi regions may have higher predicted scores for Cisplatin and Paclitaxel compared to CRGPlowepi regions (Supplementary Fig. 6D-O), consistent with the earlier single-cell analysis. Taken together, these exploratory findings suggest a possible association between CRGP status and drug sensitivity patterns; however, it is important to note that these results are based on computational predictions and lack direct experimental validation, which constitutes a limitation of this study.

Epithelial cells were stratified into two groups based on CRGP scoring: CRGP high (CRGPhighepi) and CRGP low (CRGPlowepi) (Fig. 4A). Differential enrichment analysis using Reactome, Hallmark, and KEGG pathways revealed significant upregulation of cell cycle-associated pathways in CRGPhighepi, including cell_cycle_mitotic, m_phase, g2m_checkpoint, and myc_targets, indicating enhanced proliferative capacity (Fig. 4B). Further analysis with CancerSEA across 12 tumor states showed that CRGPhighepi exhibited increased activity in pathways related to the cell cycle and metastasis, while pathways associated with differentiation and inflammation were suppressed (Fig. 4C). These findings suggest that CRGPhighepi cells are more aggressive and less differentiated, aligning with a metastatic phenotype. To explore the regulatory mechanisms driving these pathway activations (Supplementary Fig. 7 A), transcriptional regulatory analysis of NSCLC epithelial cells was conducted. Six transcriptional modules were identified through the connection specificity index (Supplementary Fig. 7B). CRGPhighepi exhibited significantly higher scores in modules 1 and 2, enriched for key regulatory factors (Supplementary Fig. 7C-D). Transcription factor activity analysis showed heightened activity of BACH1, STAT2, IRF9, KLF5, NR2C2, MAZ, and THAP1 in CRGPhighepi (Supplementary Fig. 7E). These transcription factors likely drive the upregulation of cell cycle and metastasis-related pathways, contributing to the malignant and proliferative behavior of CRGPhighepi.

Developmental hierarchy and tumor characteristics within the CRGP group

The developmental hierarchy of the CRGP group was analyzed using the Monocle algorithm for pseudotime reconstruction. Tumor stemness characteristics, assessed with the CytoTRACE algorithm, revealed significantly higher tumor stemness scores in CRGPhighepi cells compared to CRGPlowepi (Supplementary Fig. 8A-B). This positions CRGPhighepi as the developmental origin of cell trajectories, with high stemness scores reflecting early-stage dominance. Pseudotime analysis with Monocle demonstrated a dynamic decrease in CRGPhighepi cell proportions over development, indicating a transition in cellular states (Supplementary Fig. 8D-E). Genes involved in cell development were categorized into four clusters. Early-stage genes like SLC2A1 and IGFBP3 were predominantly expressed in early development, while late-stage markers such as WIF1 and LAMP3 became more prominent in later stages (Supplementary Fig. 8 F). Pseudotime analysis highlighted tumor-associated pathways, including angiogenesis (ANG), apoptosis (APO), epithelial-mesenchymal transition (EMT), PI3K, DNA repair, and CRGP (Supplementary Fig. 8G). Tumor characteristics such as DNA repair and PI3K showed a decline over pseudotime, while CRGPhighepi cells maintained elevated activity in these pathways throughout development, suggesting a sustained tumorigenic advantage.

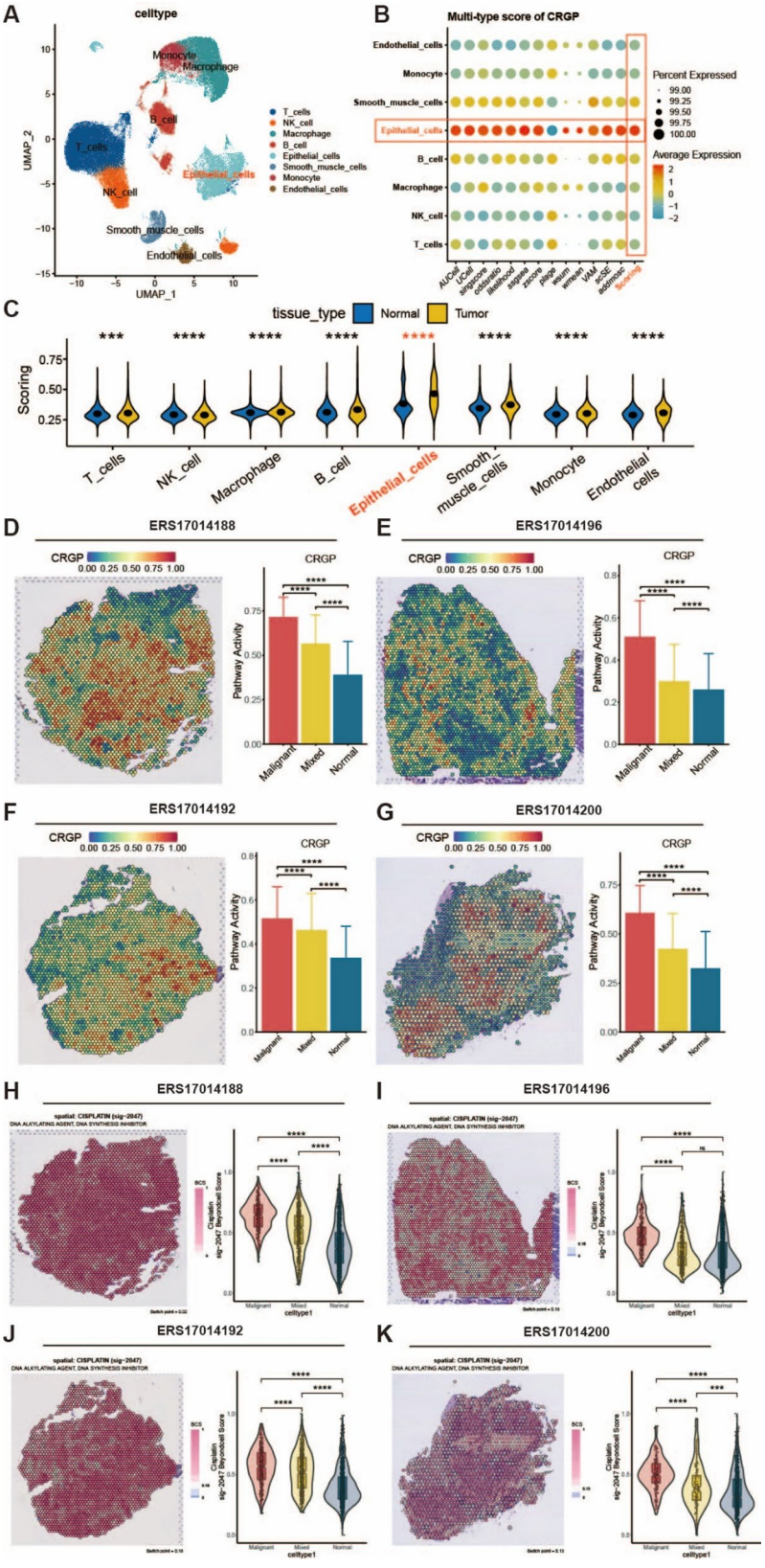

Fig. 3 (See legend on next page.)

(See figure on previous page.)

Fig. 3 The cisplatin-resistant gene panel (CRGP) is elevated in epithelial cells. (**A**) Uniform Manifold Approximation and Projection (UMAP) shows cell types after batch correction and dimensionality reduction clustering. (**B**) The bubble chart displaying the scores of the CRGP in various cell types using multiple enrichment analysis methods. (**C**) The violin plot showing the average enrichment scores of various cell types. (**D**-**G**) Enrichment scores of the CRGP in spatial transcriptomics and analysis of differences between regions. (**H**-**K**) Cisplatin drug sensitivity in spatial transcriptomics and analysis of differences between regions. ****$P < 0.0001$, ***$P < 0.001$, **$P < 0.01$, *$P < 0.05$, ns $P > 0.05$

To spatially contextualize these findings, RCTD deconvolution was used to map single-cell cohorts onto spatial transcriptomic (ST) data, revealing cell-type distributions (Supplementary Fig. 9A-D). Trajectory analysis with stLearn indicated a clear transition from CRGPhighepi to CRGPlowepi, with the trajectory tree capturing evolutionary relationships between cell clusters (Supplementary Fig. 9E-L). CRGP scores positively correlated with enrichment scores of trajectory-associated genes, reinforcing the association between CRGPhighepi and early developmental stages (Supplementary Fig. 9M-P). These results confirm CRGPhighepi as the developmental origin of the CRGP group, representing an early-stage population with high stemness and tumorigenic potential, with a gradual transition toward CRGPlowepi reflecting cellular evolution tied to developmental and spatial dynamics within the tumor microenvironment.

Metabolic landscape of the CRGP group: insights from single-cell metabolomics

Following previous findings on glycogen and pyrimidine metabolism activation in CRGPhighepi (Fig. 4B), metabolic distinctions within the CRGP group were explored using the scFEA algorithm. Of the 169 metabolic pathways analyzed, several were upregulated in CRGPhighepi, including those involved in the uptake of glycine, citrate, arginine, and fatty acids, reflecting a metabolically dynamic profile (Supplementary Fig. 4 A). In contrast, pathways upregulated in CRGPlowepi were associated with serine uptake and dCDP to dUMP conversion, indicating a different metabolic strategy (Supplementary Fig. 9 A).

Further analysis of CRGPhighepi revealed robust activation of key metabolic pathways. Pathways such as glycolysis-TCA cycle coupling demonstrated efficient energy generation, while pyrimidine and purine biosynthesis supported nucleotide production for rapid cell proliferation (Supplementary Fig. 9B-D). Propionyl-CoA metabolism, essential for fatty acid and amino acid utilization, and glycan biosynthesis were notably active (Supplementary Fig. 9E-G). This enhanced metabolic profile underscores CRGPhighepi's superior metabolic capabilities, supporting tumor growth, survival, and cisplatin resistance. The interplay between energy production, nucleotide synthesis, and glycan biosynthesis highlights the aggressive, adaptive phenotype of CRGPhighepi, suggesting potential metabolic vulnerabilities that could be targeted therapeutically.

Interaction between CRGPhighepi and smooth muscle cells

The tumor microenvironment (TME) plays a pivotal role in influencing tumor responses to treatment, serving as a dynamic center for intercellular interactions. To explore the relationships between the CRGP group and other cell types, we performed single-cell analysis of intercellular communication, revealing a notable interaction between CRGPhighepi and smooth muscle cells (Fig. 5A). These interactions were found to activate several pathways, including the EGFR tyrosine kinase inhibitor pathway, estrogen signaling pathway, endocrine resistance, FoxO signaling pathway, and focal adhesion (Fig. 5B). Ligand-receptor pairs appeared to be key elements in this communication network. Specifically, key ligand-receptor pairs from CRGPhighepi to smooth muscle cells included TGFA-EGFR, KITLG-PDGFRB, VEGFA-PDGFRA, and VEGFB-PDGFRB (Fig. 5C, Supplementary Fig. 11). Conversely, important pairs from smooth muscle cells to CRGPhighepi comprised CXCL12-CXCR4, WNT2-LRP6, CXCL14-CXCR4, WNT2-LRP5, HGF-ErbB2, and WNT2-FZD5, indicating a bidirectional communication network (Fig. 5C). To verify these interactions, spatial transcriptomics deconvolution showed notable colocalization between CRGPhighepi and smooth muscle cells (Fig. 5D-G). To validate these findings, we conducted heterotypic cellular network analysis and cellular co-localization analysis using spatial transcriptomics. We identified extensive cellular networks between CRGPhighepi and smooth muscle cells (Fig. 5H-K). Additional spatial dependency analysis using the mistyR algorithm revealed potential dependencies, extending beyond direct colocalization to neighboring and more distant regions (up to 15 spots) (Fig. 5L). These spatial relationships were consistent across multiple spatial transcriptomic samples, supporting the reliability of these findings (Supplementary Fig. 12A-B).

This analysis highlights the potential interaction between CRGPhighepi and smooth muscle cells. The various communication pathways, mediated by different ligand-receptor pairs and spatial dependencies, suggest a role for smooth muscle cells in influencing the behavior of CRGPhighepi within the TME. This interaction may provide insights into tumor progression, therapeutic resistance, and potential targeting strategies.

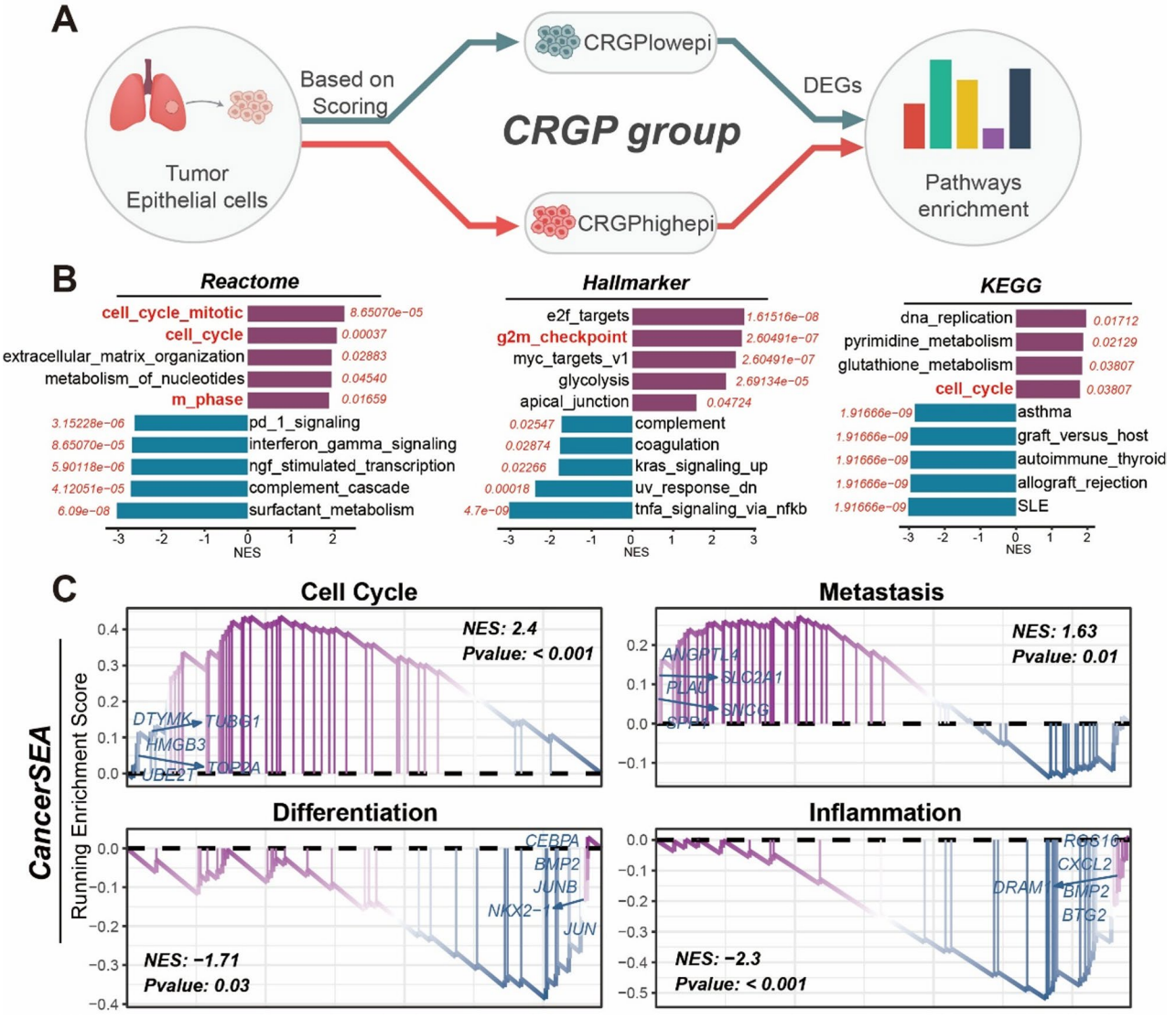

Fig. 4 Identification and functional analysis of CRGPhighepi cell population. (**A**) Schematic diagram of the identification of CRGP high score (CRGPhighepi) cell clusters. (**B**) Bar chart showing enrichment analysis of Reactome, Hallmarker, and KEGG pathways. (**C**) A line chart displaying the flow state enrichment analysis in CancerSEA

Cisplatin-resistant gene panel (CRGP): dependency on cell cycle and tumor states

Our research highlights the central role of the Cisplatin-Resistant Gene Panel (CRGP) in driving cell cycle-related pathways, a finding further validated by spatial transcriptomics analyses. Using the CancerSEA database, which includes 12 tumor cell states, we performed enrichment analyses to map the CRGP across various tumor states. Spatial transcriptomics data revealed significant enrichment of cell cycle pathways in malignant regions (Fig. 6A). Pathway dependency analysis using the mistyR algorithm showed that the CRGP is heavily dependent on cell cycle and DNA damage/repair states across spatially distinct regions, including colocalized, immediate neighborhood, and extended neighborhood (15 spots) (Fig. 6B-E). These findings were consistently validated across multiple spatial transcriptomic datasets (Supplementary Fig. 13A-C).

CRGPhighepi predominantly activates cell cycle-related pathways, a connection further confirmed by integrating spatial transcriptomics deconvolution results with tumor state enrichment analyses. CRGPhighepi exhibited pronounced activity in spatial pathways associated with DNA damage (Fig. 6F), DNA repair (Fig. 6G), cell cycle (Fig. 6H), and CRGP itself (Fig. 6H). Pathway dependency analysis using mistyR revealed that CRGPhighepi strongly relies on the CRGP, as well as on cell cycle and DNA damage/repair pathways both within and beyond its immediate spatial regions (Fig. 6I-J). These findings underscore the CRGP's reliance on tumor

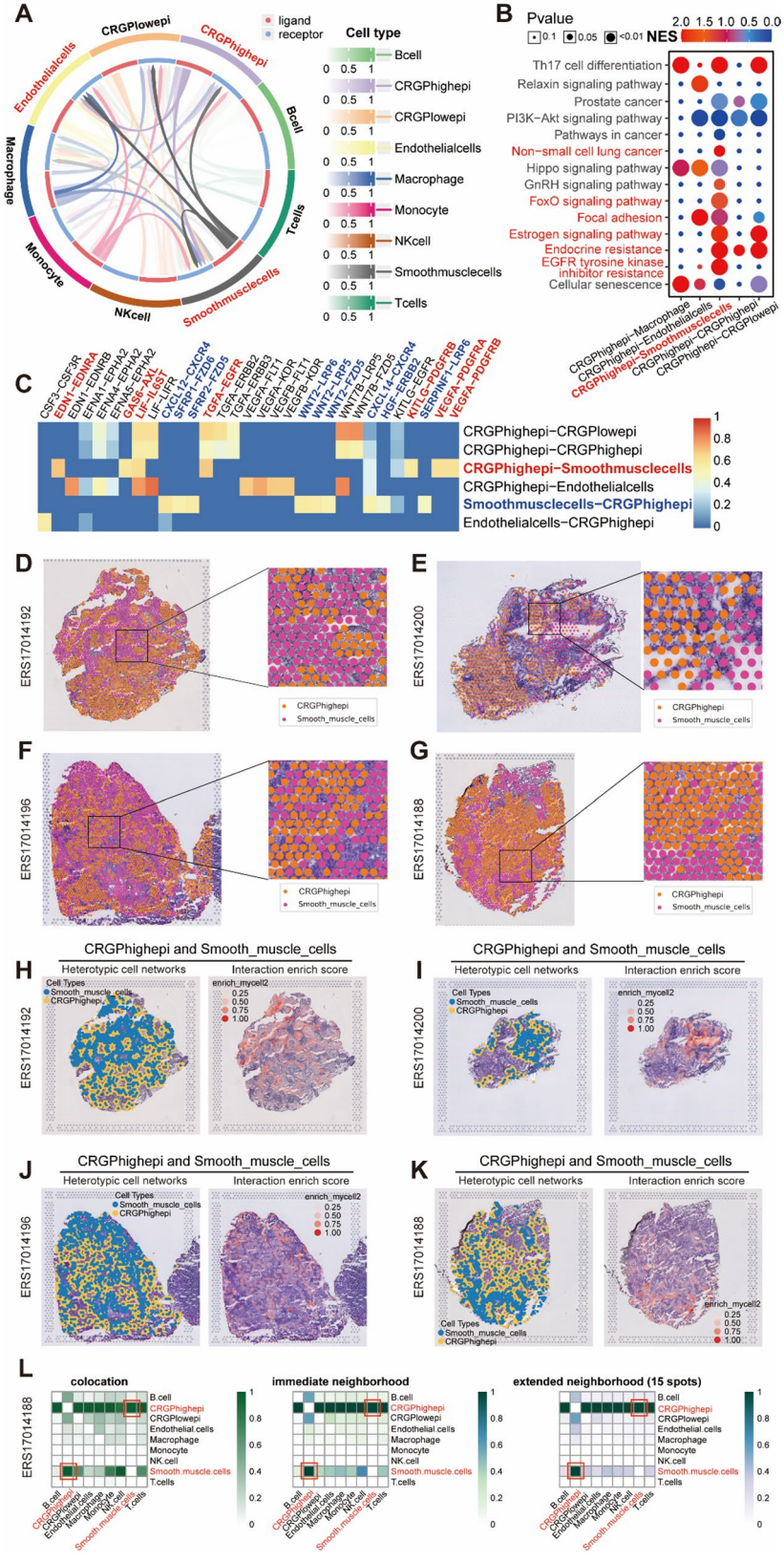

Fig. 5 (See legend on next page.)

(See figure on previous page.)

Fig. 5 Interaction between CRGP high score (CRGPhighepi) cell clusters and smooth muscle cells. (**A**) Analysis of interaction strength between CRGPhighepi and various cell types. Analysis of activated pathways (**B**) activated ligand-receptor pairs (**C**) in various cell communications. (**D**-**G**) Spatial transcriptomics deconvolution results reveal the close proximity of CRGPhighepi and Smooth muscle cells. (**H**-**K**) Spatial transcriptomics heterotypic cell network analysis shows colocalization of CRGPhighepi and smooth muscle cells. (**L**) Heatmap showing intercellular dependency analysis in the spatial transcriptomics colocation, immediate neighborhood, and extended neighborhood (15 spots) regions

states and pathways linked to cell cycle progression and genomic stability, highlighting its role in malignant progression and cisplatin resistance.

Mendelian randomization (MR) analysis: CRGP and lung cancer causality

To explore the causal relationship between CRGP-associated genetic variations and lung cancer, we performed Mendelian Randomization (MR) analysis using data from 31 Genome-Wide Association Studies (GWAS) cohorts. In the bbj-a-133 cohort, genes such as CPD, MYO1D, and SLC2A1 were identified as causal factors for lung cancer (Supplementary Fig. 14 A, C). In the ebi-a-GCST90018655 cohort, genes including C1QTNF6, RCC2, and PODXL2 showed a significant causal link to lung cancer (Supplementary Fig. 14B, D). Across all 31 GWAS cohorts, 171 genes were determined to have a causal relationship with lung cancer (Supplementary Table 3). This large-scale analysis provides strong evidence for the genetic basis of CRGP's involvement in lung cancer pathogenesis, identifying key genetic drivers that may play pivotal roles in tumor development and cisplatin resistance.

Robust machine learning model predicts patient survival and guides treatment

We used the FindMarker function to analyze CRGPhighepi and identified marker genes with |logFC| > 0.5. These genes were intersected with the results from Mendelian randomization (MR) analysis, and the resulting genes were used to construct a prognostic model (Supplementary Fig. 15, Supplementary Table 5). Survival prediction was performed using various machine learning algorithms, with SuperPC ranking among the top three for mean C-index (Supplementary Fig. 16 A). Its superior ability to retain more genes compared to other methods (Supplementary Fig. 17) made it the optimal choice for building the SuperPCCRGP model. The median SuperPCCRGP score was used to categorize patients into high-risk and low-risk groups. Across datasets, including the TCGA training dataset and six independent validation sets, the high-risk group consistently had poorer survival outcomes compared to the low-risk group (Supplementary Fig. 16B-H). ROC analysis further supported SuperPCCRGP's predictive strength, with AUC values of 0.62, 0.61, 0.62, 0.62, and 0.57 for 1- to 5-year survival rates in the TCGA-NSCLC dataset. In other cohorts such as GSE11969, GSE12428, and GSE31210, AUC values ranged from 0.56 to 0.81, confirming the model's robust performance across independent datasets (Supplementary Fig. 16I-M). These results establish SuperPCCRGP as a reliable tool for survival prediction in NSCLC. SuperPCCRGP consistently outperformed other prognostic models, achieving the highest C-index in all independent cohorts (Supplementary Fig. 18 A). Using the median SuperPCCRGP value as a cutoff, risk groups were linked to clinical indicators, showing significant differences in survival status, tumor grade, stage, and T stage (Supplementary Fig. 18B). The high-risk group had a higher prevalence of tumor grades 2–4, with SuperPCCRGP predicting shorter survival times (Supplementary Fig. 18C-D). Univariate and multivariate Cox regression analyses using the TCGA-NSCLC dataset confirmed SuperPCCRGP as a significant risk factor for overall survival (OS), progression-free interval (PFI), and disease-specific survival (DSS) (Supplementary Fig. 18E-J). SuperPCCRGP was found to be a significant risk factor in both univariate ($HR > 1$, $p < 0.001$) and multivariate analyses for OS (HR: 1.476, $p < 0.001$), PFI (HR: 1.471, $p < 0.001$), and DSS (HR: 1.780, $p < 0.001$), solidifying its role as a powerful prognostic marker in NSCLC.

Submap analysis revealed that high-risk patients had better responses to immune therapy, particularly in the TCGA and GSE31210 cohorts (Supplementary Fig. 19A-B). Further analysis of publicly available single-cell immune therapy datasets showed that immune-responsive cells had higher risk scores (Supplementary Fig. 19C-E). Additionally, data from the CTRP and PRISM databases indicated that high-risk patients were more sensitive to drugs such as alectinib, docetaxel, erlotinib, and gefitinib (Supplementary Fig. 19F-I). Promising drug candidates for high-risk patients, including dasatinib, pluripotin, cephalomannine, and epothilone-b, were also identified (Supplementary Fig. 19J-K). In conclusion, SuperPCCRGP provides an accurate prognostic model for predicting survival and offers a personalized approach for treatment strategies in NSCLC, improving therapeutic outcomes and guiding drug choices based on individual risk profiles.

Lysyl oxidase homolog 2 increases cell proliferation and chemoresistance

Prognostic analysis of genes retained by the SuperPC model in LUAD and LUSC identified LOXL2 and paraoxonase 2 (PON2) as risk factors in both cancer types (Supplementary Fig. 20 A). Treatment outcome analysis

showed that LOXL2 expression was higher in LUAD patients with stable disease and higher in patients with progressive disease than in those with complete remission/response. In LUSC, LOXL2 expression was higher in stable disease compared to complete remission/response (Supplementary Fig. 20B-C), indicating a strong correlation between LOXL2 expression and treatment response. However, PON2 expression did not significantly differ among treatment groups in LUAD and LUSC (Supplementary Fig. 20D-E). Further analysis of LOXL2 expression revealed higher levels in tumor tissues compared to normal tissues in proteomics cohorts (LUAD_CPTAC and LUSC_CPTAC) (Supplementary Fig. 21A-B). Validation cohorts (GSE31547, GSE40791, GSE21933, GSE33479) confirmed higher LOXL2 expression in tumor tissues (Supplementary Fig. 21C-F). Additionally, higher LOXL2 expression in proteomics cohorts was associated with shorter survival durations (Supplementary Fig. 21G-H). These results establish LOXL2 as a risk factor in NSCLC and a predictor of clinical treatment response.

To further investigate the relationship among CRGP, LOXL2, and cisplatin resistance, we performed weighted gene co-expression network analysis (WGCNA) on the GSE21656 dataset. Genes were clustered into multiple modules (including MEdarkgrey, MEgrey, MEdarkgreen, MEmagenta, and MEnavajowhite) using a dynamic tree-cutting algorithm (Supplementary Fig. 22 A). Among these, the MEdarkgreen and MEpaleturquoise modules showed significant correlations with the cisplatin-resistant phenotype, while the MEivory module was associated with the Q1 trait (top 25% LOXL2 expression; Supplementary Fig. 22B). Intermodular gene relationships are illustrated in Supplementary Fig. 22C. Notably, CRGP genes were most enriched within the MEdarkgreen module (88.6%), followed by MEnavajowhite2 and MEgrey (Supplementary Fig. 22D and Supplementary Table 6). We therefore focused on correlating genes within the MEdarkgreen module with the Q1 trait to elucidate the link between CRGP and LOXL2. The MEdarkgreen module exhibited a strong positive correlation with cisplatin resistance (cor = 0.95, $p < 1 \times 10^{-200}$; Supplementary Fig. 22E) and a moderate correlation with the Q1 trait (cor = 0.55, $p < 1 \times 10^{-200}$; Supplementary Fig. 22 F). Functional enrichment analysis revealed that the MEdarkgreen module was primarily involved in DNA replication and cell cycle pathways, MEnavajowhite2 in tyrosine metabolic process, MEivory in regulation of DNA repair and synaptic vesicle recycling, and MEskyblue in embryonic placenta development (Supplementary Fig. 22G-J). Protein-protein interaction (PPI) analysis of CRGP-related genes within the MEdarkgreen module via the STRING database (Supplementary Fig. 23) identified strong interactions among core genes such as TOP2A, BRCA1, and CDC6. LOXL2 was located at key hubs within this network, suggesting its central role in mediating cisplatin resistance through CRGP. To further validate the relationship between CRGP and LOXL2 at single-cell resolution, we first assessed LOXL2 expression patterns and found it predominantly expressed in tumor epithelial cells, with lower levels in smooth muscle and endothelial cells (Supplementary Fig. 24 A). Tumor epithelial cells were then categorized into LOXL2posEpi (LOXL2-positive epithelial cells) and LOXL2negEpi (LOXL2-negative epithelial cells) subsets based on LOXL2 expression. CRGP scores were significantly higher in LOXL2posEpi compared to LOXL2negEpi cells (Supplementary Fig. 24B). The mRNAs of the key CRGP genes all show strong correlations with the mRNA expression of LOXL2 (ABCC2 (cor = 0.56, $p < 0.05$); BRCA1 (cor = 0.68, $p < 0.05$); TOP2A (cor = 0.46, $p < 0.05$); and CDC6 (cor = 0.62, $p < 0.05$)) (Supplementary Fig. 24C–F). Collectively, these findings suggest that LOXL2 serves as a core regulator within the CRGP network, contributing critically to the cisplatin-resistant phenotype.

In vitro experiments were conducted to assess the biological functions of LOXL2. Immunofluorescence staining of LOXL2 in H520 and PC9 cells revealed its predominant nuclear localization (Fig. 7A). LOXL2 expression was knocked down in both cell lines using siRNAs, and Western blot analysis confirmed successful knockdown (Fig. 7B). Following LOXL2 knockdown, EdU assays showed reduced cell proliferation (Fig. 7C-D) and viability (Fig. 7E-F). Additionally, invasion assays demonstrated a significant reduction in migration ability in both cell lines after LOXL2 knockdown (Fig. 7G-I). These results suggest that LOXL2 promotes proliferation and migration in NSCLC cells.

To explore the relationship between LOXL2 and chemotherapy, we assessed cell viability after LOXL2 knockdown under cisplatin treatment. LOXL2 knockdown significantly reduced cell viability under cisplatin treatment (Fig. 8A-B). Clonogenic assays revealed that LOXL2 knockdown inhibited colony formation and increased cisplatin sensitivity (Fig. 8C-E). Western blot analysis showed that LOXL2 knockdown, followed by cisplatin treatment, reduced CyclinD1, CyclinE1, and CDK4 expression while increasing P21 expression (Fig. 8F-I). These findings align with previous research linking cell cycle regulation to CRGP.

Furthermore, we also observed that LOXL2 influences DNA damage repair markers. Knockdown of LOXL2 inhibited the expression of γ-H2AX protein, a marker for DNA damage, following cisplatin treatment (Fig. 9A-D). Immunofluorescence analysis showed reduced γ-H2AX intensity in the LOXL2 knockdown group after cisplatin treatment (Fig. 9E-F). This is consistent with our previous findings linking DNA damage repair to the

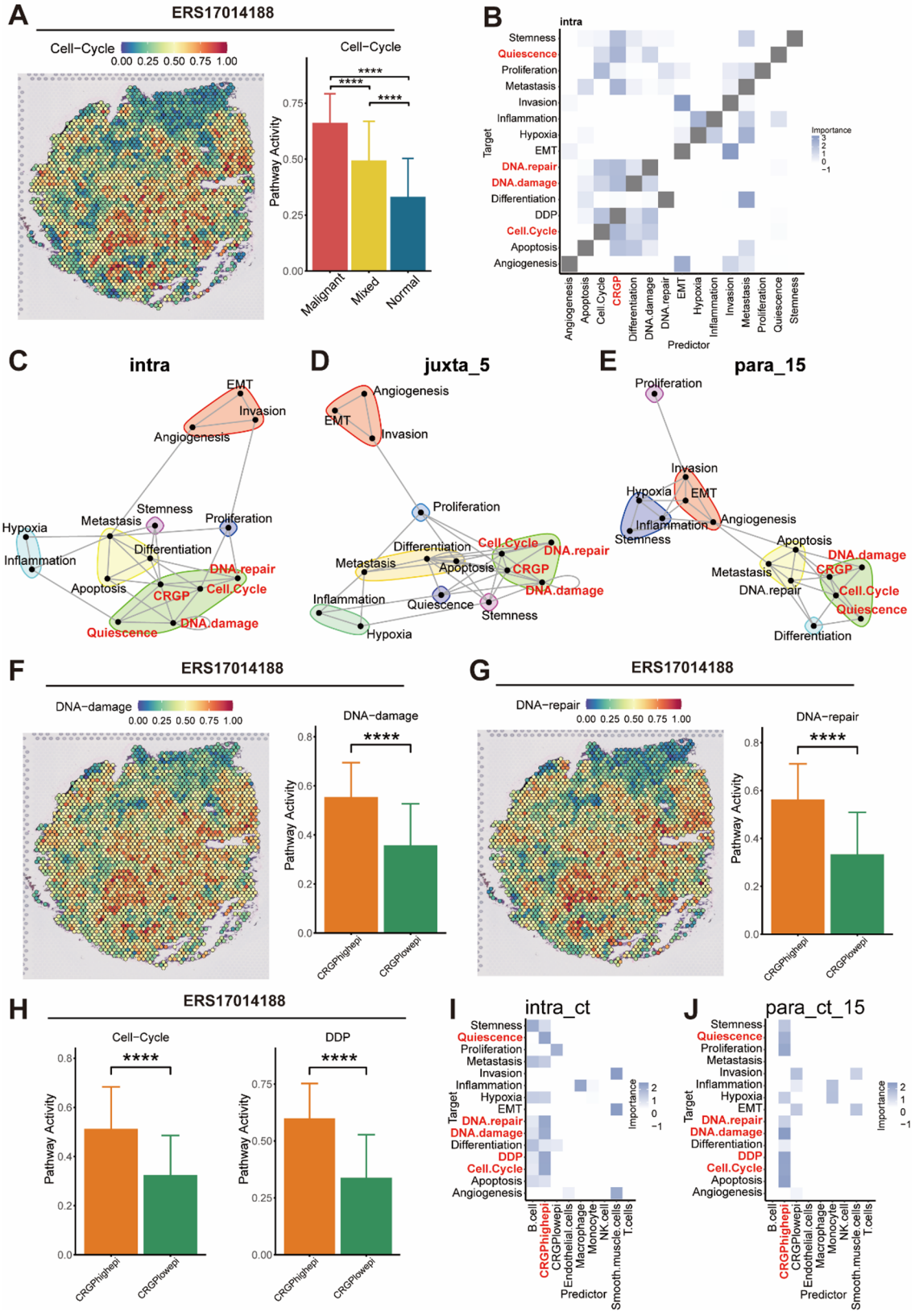

Fig. 6 Exploration of pathways related to the cisplatin-resistant gene panel (CRGP) in spatial transcriptomics (STs). (**A**) Enrichment results of the cell cycle pathway in STs and comparison of differences between regions. (**B**) Heatmap showing the cell pathways dependent on the CRGP within the intra region in a spatial context. (**C**-**E**) Network diagrams showing the cell pathways dependent on the CRGP in the intra (**C**), juxta_5 (**D**), and para_15 (**E**) regions in a spatial context. ****$P < 0.0001$, ***$P < 0.001$, **$P < 0.01$, *$P < 0.05$, ns $P > 0.05$

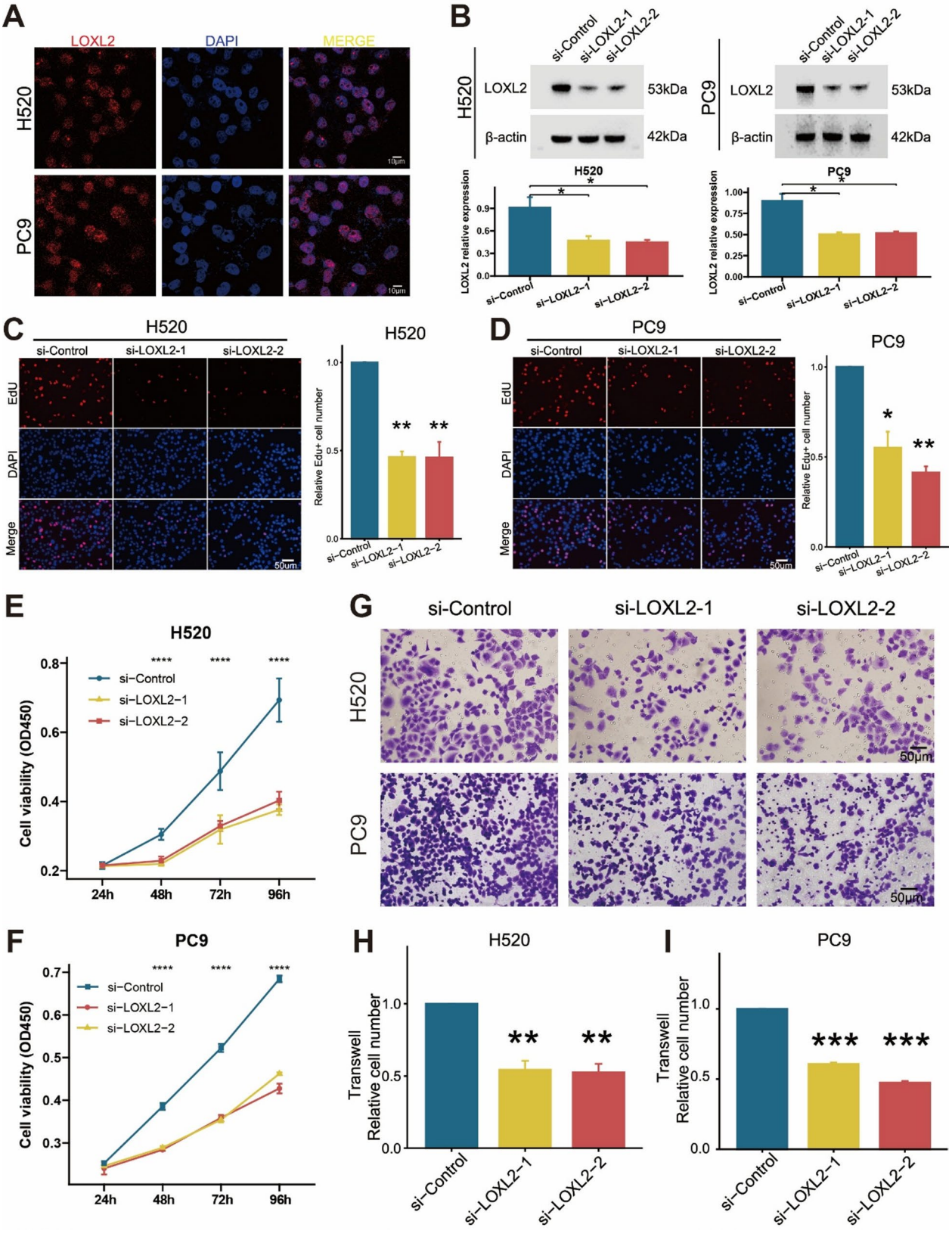

Fig. 7 (See legend on next page.)

(See figure on previous page.)

Fig. 7 Knockdown of lysyl oxidase homolog 2 (LOXL2) inhibits NSCLC cell proliferation. (**A**) Immunofluorescence analysis of LOXL2 localization in H520 and PC9 cells. (**B**) Western blot showing the efficiency of LOXL2 knockdown and its statistical analysis in a bar chart. (**C**-**D**) The effect of LOXL2 knockdown on cell DNA synthesis is shown here through EdU assay. (**E**-**F**) The impact of downregulated LOXL2 on cell viability shown through Cell Counting Kit 8 assay. (**G**-**I**) The impact of downregulated LOXL2 knockdown on cell invasion is shown here through Transwell assay and its statistical analysis is presented in the bar chart. ****$P < 0.0001$, ***$P < 0.001$, **$P < 0.01$, *$P < 0.05$, ns $P > 0.05$

cisplatin-resistant gene panel (CRGP). In summary, this study demonstrates that LOXL2 enhances cell proliferation and chemoresistance, making it a potential novel target for clinical chemotherapy. However, our experiment has some limitations, and further validation through rescue experiments and in vivo studies is required.

Discussion

Cisplatin-based compounds are commonly used in the treatment and adjuvant chemotherapy of advanced non-small cell lung cancer (NSCLC). However, cisplatin resistance severely impacts the efficacy of chemotherapy and patient prognosis [1, 2]. In recent years, the application of single-cell and spatial transcriptomics technologies has revealed some of the mechanisms underlying cisplatin resistance in NSCLC.

Our study indicates that the gene panel for cisplatin chemotherapy resistance is mainly associated with pathways involved in the cell cycle and DNA damage repair. Abnormal regulation of cell cycle and DNA damage repair plays a crucial role in NSCLC cisplatin resistance. For example, in the cisplatin-resistant NSCLC cell line A549rCDDP2000, cisplatin no longer causes G2/M phase cell cycle arrest [11]. When compared with cisplatin-sensitive A549 cells, these resistant cells show lower levels of apoptosis, even though the amount of platinum-DNA adducts is similar[11].This indicates that changes in cell cycle control may play a role in reducing apoptosis triggered by cisplatin.

Our analysis identified potential interactions between CRGPhighepi and smooth muscle cells. However, our study was limited to exploring correlations and lacked experimental validation, thus presenting certain limitations. In fact, related research indicates that smooth muscle cells function in cisplatin resistance. Smooth muscle cells secrete a variety of cytokines and growth factors, containing TGF-β, PDGF, and VEGF, which can activate signaling pathways, enhancing DNA damage repair capabilities in tumor cells. For instance, TGF-β could enhance DNA repair capabilities in tumor cells through Smad and non-Smad pathways, reducing cisplatin-induced DNA damage, thereby increasing cell survival rates [35]. Second, VEGF-C enhances the invasiveness of gastric cancer cells and confers resistance to cisplatin in RhoGDI2-overexpressing cells [36]. Smooth muscle cells can interact directly with cancer cells and promote drug resistance through cell-cell contact and changes in extracellular matrix components [37]. The presence of smooth muscle cells in the tumor microenvironment may also indirectly affect the efficacy cisplatin by altering angiogenesis and oxygen supply. Factors secreted by smooth muscle cells, such as VEGF, can promote angiogenesis, improving blood supply and oxygen levels within tumors, thus reducing the effectiveness of cisplatin [38]. In conclusion, smooth muscle cells influence cisplatin resistance of NSCLC through multiple mechanisms. Studying these mechanisms in depth will aids in understanding the complexity of cisplatin resistance and provide important clues for developing new therapeutic strategies.

Our research shows that LOXL2 is associated with the clinical treatment response of NSCLC cells. We confirmed through laboratory experiments that LOXL2 promotes the proliferation of NSCLC cells, while downregulation of LOXL2 enhances the sensitivity of these cells to cisplatin chemotherapy. Our study revealed that knockdown of LOXL2 leads to a reduction in the expression of Cyclin D1, Cyclin E1, and CDK4, while increasing the expression of P21. This indicates the critical role of cell cycle-related genes in cisplatin resistance. Specifically, the upregulation of Cyclin D1, Cyclin E1, and CDK4, coupled with the downregulation of P21, forms a key molecular loop driving drug resistance. In cervical cancer, the aberrant activation of the P16INK4A/CDK4/pRb pathway is the core mechanism of cisplatin resistance. Upregulation of P16INK4A in resistant cells interacts with CDK4 to inactivate pRb, promoting proliferation and resistance to apoptosis. Knockdown of P16INK4A can reverse this effect and enhance cisplatin-induced apoptosis [39]. In lung cancer, the upregulation of SSDBP1 induces resistance by promoting Cyclin D1 expression [40]. Conversely, miR-381 increases cisplatin sensitivity by targeting Cyclin D1 and CDK4, while simultaneously upregulating P21 expression to block the cell cycle in the G0/G1 phase [41]. This finding is corroborated in liver cancer, where miR-34a overcomes chemotherapy resistance by downregulating Cyclin D1 and CDK4 [42]. Moreover, in rectal cancer, the LINC00461/miR-593-5p/CCND1 axis further expands the upstream regulatory network of Cyclin D1, demonstrating that non-coding RNAs mediate drug resistance through fine regulation of Cyclin D1 expression [43]. Cyclin E1 also plays a significant role in cisplatin resistance across various cancers. In bladder cancer resistant cells, CCNE1 is significantly upregulated [44]. In small cell lung cancer, FIGNL1 affects chemotherapy sensitivity by regulating Cyclin E1 and CDK2 [45]. In ovarian cancer,

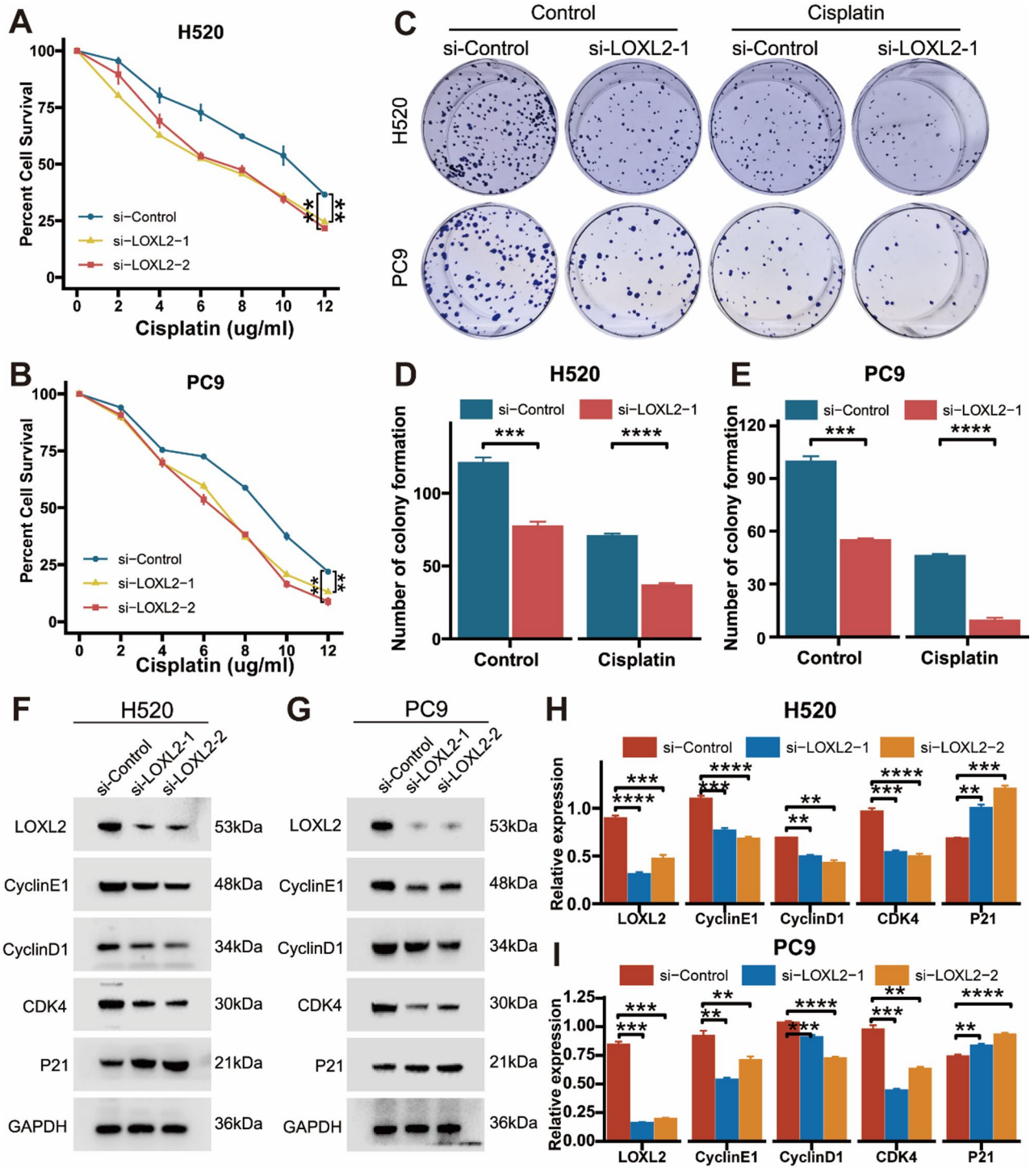

Fig. 8 Knockdown of lysyl oxidase homolog 2 (LOXL2) significantly inhibits cell proliferation under cisplatin treatment. Knockdown of LOXL2 inhibits (**A**-**B**) cell viability under cisplatin treatment and (**C**-**E**) cell colony formation ability under cisplatin treatment and its statistical analysis is presented in a bar chart form. (**F**-**I**) LOXL2 knockdown under cisplatin treatment inhibits the expression of cyclinD1, cyclinE1, and cyclin-dependent kinase 4 (CDK4), increases the expression of P21; their statistical analysis is presented in a bar chart. ****$P < 0.0001$, ***$P < 0.001$, **$P < 0.01$, *$P < 0.05$, ns $P > 0.05$

triple-negative breast cancer, and pancreatic cancer, aberrant expression of Cyclin E1 is associated with poor prognosis and a drug-resistant phenotype [46–48]. Studies in glioblastoma suggest that targeting Cyclin E1 with miR-497/MIR497HG may represent a new sensitization strategy [49]. Notably, CDK4, a key partner kinase of Cyclin D1, is regulated by multiple synergistic mechanisms. For example, in ovarian cancer, ACLY regulates

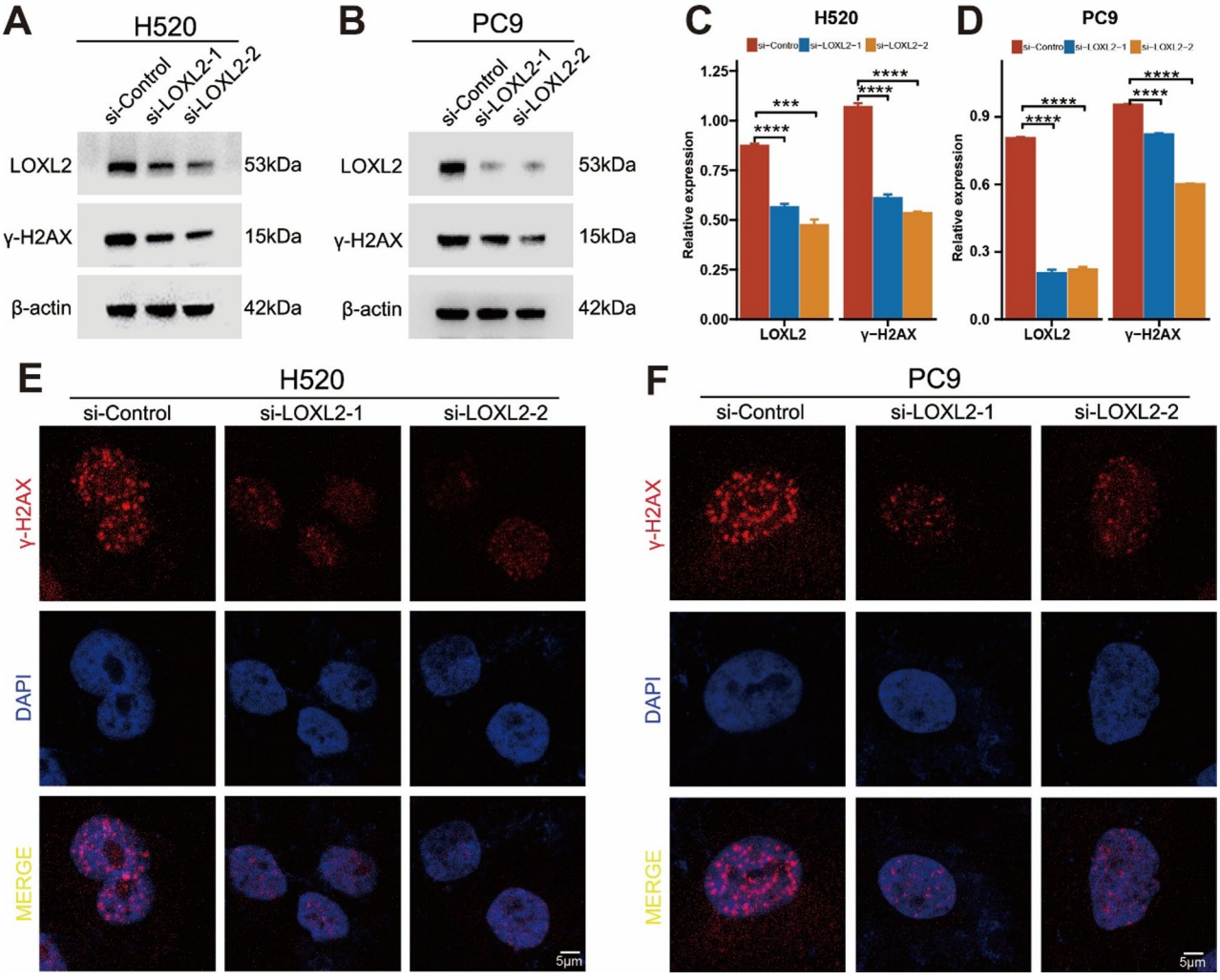

Fig. 9 Knockdown of lysyl oxidase homolog 2 (LOXL2) significantly inhibits DNA damage repair under cisplatin treatment. (**A**-**D**) The effect of LOXL2 knockdown on γ-H2AX under cisplatin treatment was analyzed by Western blotting (statistical analysis is presented in the bar chart). (**E**-**F**) The effect of LOXL2 knockdown on γ-H2AX under cisplatin treatment was analyzed by immunofluorescence. ****$P < 0.0001$, ***$P < 0.001$, **$P < 0.01$, *$P < 0.05$, ns $P > 0.05$

the P16-CDK4-CCND1 pathway to affect cisplatin sensitivity [50], while in non-small cell lung cancer, garcinia acid induces cell cycle arrest and apoptosis by downregulating CDK4 and upregulating p53 and P21 [51]. In contrast, P21, a negative regulator of the cell cycle, is commonly downregulated in drug-resistant settings. Its loss of function further exacerbates the dysregulation of the cell cycle. For instance, in non-small cell lung cancer, miR-381 enhances cisplatin toxicity by upregulating P21 [41]. In ovarian cancer, 53BP1 and ENO1 regulate chemotherapy sensitivity and senescence by modulating P21 expression or restoring the P21/p53 axis [52, 53].

Studies have demonstrated that overexpression of LOXL2 links to invasiveness and poor prognosis in tumors like NSCLC, breast cancer, and esophageal squamous cell carcinoma [54]. Prognostic analysis identified that LOXL2 is a risk factor for NSCLC. Our experiments further confirmed that under cisplatin treatment, LOXL2 can inhibit cell cycle-related proteins and suppress DNA damage repair. The above analysis suggests that LOXL2 may be an important target for altering the sensitivity of NSCLC to cisplatin chemotherapy. However, our study has several limitations. First, it was confined to *in vitro* experiments, and no in vivo validation was performed to confirm the role of LOXL2 in modulating cisplatin sensitivity. Second, functional rescue experiments are lacking; we did not determine whether exogenous overexpression of LOXL2 can convert CRGPlowepi cells-which exhibit a low CRGP score and are cisplatin-sensitive-into CRGPhighepi cells characterized by high drug resistance and high proliferative capacity. Third, we did not perform LOXL2 knockout experiments to examine overall changes in CRGP activity or investigate the functional role of LOXL2 in single-cell subpopulations, and these

findings lack experimental validation. In addition, the combined effect of LOXL2 inhibitors and cisplatin has not yet been investigated. In the future, the therapeutic synergy between LOXL2 inhibitors and cisplatin should be explored to assess its potential for clinical translation.

Conclusion

Our study indicates that CRGP is primarily associated with pathways related to the cell cycle and DNA damage repair. Tumor epithelial cells with high CRGP scores (CRGPhighepi) interact with smooth muscle cells in spatial transcriptomics and depend on pathways related to the cell cycle and DNA damage repair. Furthermore, LOXL2 is a significant risk factor for NSCLC prognosis and an effective target for enhancing sensitivity to cisplatin chemotherapy.

Supplementary Information

The online version contains supplementary material available at https://doi.org/10.1186/s12935-026-04170-0.

Supplementary Material 1: Fig. 1. IC50 Curves of H520 Parental Cells and Cisplatin-Resistant Cells

Supplementary Material 2: Fig. 2. The UMAP dimensionality reduction plot of the integrated data from 5 NSCLC single-cell cohorts

Supplementary Material 3: Fig. 3. Spatial transcriptomics identifying benign and malignant regions based on the R package Cottrazm (A-D) Spatial transcriptomics division of benign and malignant regions

Supplementary Material 4: Fig. 4. Identification of potential drugs sensitive to CRGPhighepi (A) Schematic diagram of drug sensitivity grouping: tumor epithelial cells are divided into two groups based on CRGP score, along with the assessment of drug sensitivity and related pathways. (B) Exploration of potential drugs for CRGPhighepi cells using the BeyondCell algorithm. (C-D) Distribution histogram and violin plot of BeyondCell scores for Cisplatin. (E) Violin plot of BeyondCell scores for Paclitaxel. (F-G) Distribution histogram and violin plot of BeyondCell scores for CDK1-5 inhibitors. (H) Violin plot of BeyondCell scores for Su-11274. (I-J) Distribution histogram and violin plot of BeyondCell scores for Fenretinide. (K) Violin plot of BeyondCell scores for Trapidil. ****$P < 0.0001$, ***$P < 0.001$, **$P < 0.01$, *$P < 0.05$, ns $P > 0.05$.

Supplementary Material 5: Fig. 5. Cell Type-Related drug sensitivity pathway analysis (A) Drug Sensitivity Grouping Diagram: Tumor epithelial cells are divided into two groups based on CRGP scores, while evaluating pathways associated with drug sensitivity. (L-M) UMAP plot and violin plot of BeyondCell scores for the sig_G1S_WHITFIELD pathway. (N-O) UMAP plot and violin plot of BeyondCell scores for the sig_cell_cycle_CancerSEA pathway. (P-Q) UMAP plot and violin plot of BeyondCell scores for the sig_proliferation_CancerSEA pathway. (R-S) UMAP plot and violin plot of BeyondCell scores for the sig_DNA_damage_CancerSEA pathway. ****$P < 0.0001$, ***$P < 0.001$, **$P < 0.01$, *$P < 0.05$, ns $P > 0.05$.

Supplementary Material 6: Fig. 6. Spatial transcriptomics cell annotation and drug sensitivity analysis(A) Drug Sensitivity Grouping Diagram: Tumor epithelial cells are divided into two groups based on CRGP scores, while evaluating pathways associated with drug sensitivity. (L-M) UMAP plot and violin plot of BeyondCell scores for the sig_G1S_WHITFIELD pathway. (N-O) UMAP plot and violin plot of BeyondCell scores for the sig_cell_cycle_CancerSEA pathway. (P-Q) UMAP plot and violin plot of BeyondCell scores for the sig_proliferation_CancerSEA pathway. (R-S) UMAP plot and violin plot of BeyondCell scores for the sig_DNA_damage_CancerSEA pathway. ****$P < 0.0001$, ***$P < 0.001$, **$P < 0.01$, *$P < 0.05$, ns $P > 0.05$.

Supplementary Material 7:Fig.7. Transcription factor activity analysis of the CRGPhighepi cell cluster(A) Schematic diagram of transcription factor analysis in CRGP high-scoring (CRGPhighepi) cell clusters. (B) Regulon module analysis of epithelial cells. (C-D) Differential comparison of regulon modules in the cisplatin-resistant gene panel (CRGP) group. (E) Heatmap showing the activity of different transcription factors in the CRGP group (red text: higher activity of the transcription factor in CRGPhighepi; blue text: higher activity of the TF in CRGPlowepi). ****$P < 0.0001$, ***$P < 0.001$, **$P < 0.01$, *$P < 0.05$, ns $P > 0.05$.

Supplementary Material 8:Fig.8. Exploring the cell origin of the cisplatin-resistant gene panel(CRGP) group at the single-cell level. (A) CytoTRACE analysis of the differentiation potential of cells in the CRGP group. (B) Grouping of the CRGP group. (C) Raincloud plot showing the differential comparison of CytoTRACE scores. (D-E) Analysis and display of the proportion of cell types along the cellular developmental trajectory in the CRGP group. (F) Pseudotime analysis of genes related to cell development pathways. (G) Comparative pseudotime analysis of tumor activity-related pathways. ****$P < 0.0001$, ***$P < 0.001$, **$P < 0.01$, *$P < 0.05$, ns $P > 0.05$.

Supplementary Material 9:Fig.9. Exploring the cell origin of the cisplatin-resistant gene panel(CRGP) group through spatial transcriptomics (ST). (A-D) Cell types after deconvolution of the STs. (E-F) Cellular developmental trajectory and developmental trajectory tree of ST ERS17014188. (G-H) Cellular developmental trajectory and developmental trajectory tree of ST ERS17014192. (I-J) Cellular developmental trajectory and developmental trajectory tree of ST ERS17014196. (K-L) Cellular developmental trajectory and developmental trajectory tree of ST ERS17214200. (M-P) Scatter plots showing the correlation between cisplatin-resistant gene panel scores and developmental trajectory genes

Supplementary Material 10:Fig.10. Exploring metabolomic differences in the cisplatin-resistant gene panel(CRGP) group at the single-cell level. (A) A heatmap showing differences in metabolic conversion-related pathways in the CRGP group (red text: higher activity of the pathway in CRGPhighepi; blue text: higher activity of the pathway in CRGPlowepi). (B-G) Cohen's D differential analysis in glycolysis and tricarboxylic acid cycle (B), pyrimidine synthesis (C), purine synthesis (D), propionyl-CoA metabolism (E), N-linked glycan synthesis (F), and O-linked glycan synthesis (G).

Supplementary Material 11: Fig. 11. Ligand-receptor analysis of cell communication between CRGPhighepi and smooth muscle cells

Supplementary Material 12:Fig.12. Spatial transcriptomics cell dependency analysis(A-C) Heatmaps showing intercellular dependency analysis in spatial transcriptomics colocation, immediate neighborhood, and extended neighborhood (15 spots) regions

Supplementary Material 13 Fig.13. Spatial transcriptomics pathway dependency analysis(A-C) Network diagrams showing the cell pathways dependent on the cisplatin-resistant gene panel in the intra, juxta_5, and para_15 regions in the spatial context

Supplementary Material 14:Fig.14. Mendelian randomization (MR) exploring the causal relationship between cisplatin-resistant genes and lung cancer(A-B) Forest plots showing the results of MR analysis of cisplatin-resistant genes. (C-D) Volcano plots showing expression quantitative trait loci (eQTL) results of cisplatin-resistant genes

Supplementary Material 15:Fig.15. The intersection of CRGPhighepi and genes filtered by Mendelian randomization for the construction of a prognostic model (ML.genes)

Supplementary Material 16:Fig.16. Construction of prognostic models using various machine learning combinations(A) Heatmap showing the C-index of various machine learning combinations. (B-H) Survival curves of prognostic models established by the SuperPC method in different cohorts. (I-M) Area under the curve values determined using the prognostic models established by the SuperPC method for 1, 2, 3, 4, and 5-year survival durations in different cohorts

Supplementary Material 17:Fig.17. Weight analysis of genes in prognostic models established by the SuperPC method

Supplementary Material 18:Fig.18. Impact of risk scores on clinical factors(A) Comparative analysis of prognostic models established by the SuperPC method. (B) The impact of risk scores on patient survival, tumor grading, staging, and TNM classification. (C) Relationship between

risk scores and tumor grading. (D) Survival curves based on risk scores of patients with tumor grades 2–4. (E-G) Univariate analysis and (H-J) Multivariate analysis of the impact of risk scores and clinical indicators on OS, PFI, and DSS

Supplementary Material 19: Fig.19. Relationship between risk scores and clinical treatment(A-B) Prediction of response to immunotherapy based on high- and low-risk scores in TCGA and GSE31210 cohorts. (C-E) Relationship between risk scores and treatment response in single-cell immunotherapy cohorts BCC_GSE123813 (C), BLCA_GSE145281 (D), and SCC_GSE123813 (E). (F-I) Drug sensitivity analysis for alectinib (F), docetaxel (G), erlotinib (H), and gefitinib (I) in risk score groups. (J-K) Analysis of potential small molecule drugs based on high- and low-risk score groups. ****$P<0.0001$, ***$P<0.001$, **$P<0.01$, *$P<0.05$, ns $P>0.05$.

Supplementary Material 20:Fig.20. Screening of drug resistance-related genes(A) Analysis of each gene in the prognostic model established by the SuperPC method. (B) Relationship between lysyl oxidase homolog 2 (LOXL2) expression and treatment response in LUAD. (C) Relationship between LOXL2 expression and treatment response in LUSC. (D-E) Relationship between paraoxonase 2 (PON2) expression and treatment response in (D) LUAD and in (E) LUSC. ****$P<0.0001$, ***$P<0.001$, **$P<0.01$, *$P<0.05$, ns $P>0.05$.

Supplementary Material 21:Fig.21. Lysyl oxidase homolog 2 (LOXL2) expression and prognostic analysisAnalysis of LOXL2 expression in normal and tumor tissues in the (A) LUAD proteomics cohort and (B) in the LUSC proteomics cohort. Analysis of LOXL2 expression in normal and tumor tissues in (C-D) LUAD in the GSE31547 and GSE40791 cohorts and (E-F) LUSC in the GSE21933 and GSE33479 cohorts. (G-H) Survival curves showing the impact of LOXL2 expression on prognosis in LUAD and LUSC proteomics cohorts. ****$P<0.0001$, ***$P<0.001$, **$P<0.01$, *$P<0.05$, ns $P>0.05$.

Supplementary Material 22:Fig.22. Co-expression network analysis of the Cisplatin-Resistant gene panel (CRGP)(A) Identification of gene modules and their trait associations. (B) Correlation between module eigengenes and clinical traits. (C) Network diagram depicting interactions among gene co-expression modules. (D) Distribution of CRGP genes across identified modules. (E) Correlation of the MEdarkgreen module with the cisplatin resistance trait. (F) Correlation of the MEdarkgreen module with the Q1 trait (top 25% LOXL2 expression). (G-J) Functional enrichment analysis of the MEdarkgreen, MEnavajowhite2, MEivory, and MEskyblue modules

Supplementary Material 23:Fig.23. Protein-protein interaction network of CRGP-associated genes within the MEdarkgreen module

Supplementary Material 24:Fig.24. Single-cell analysis of Lysyl oxidase homolog 2 (LOXL2) expression(A) LOXL2 expression levels across major cell types. (B) Comparison of CRGP scores between LOXL2posEpi and LOXL2negEpi cells. (C–F) The mRNA correlations between ABCC2 (C), BRCA1 (D), TOP2A (E), CDC6 (F) and LOXL2 in the single-cell cohort

Supplementary Material 25:Table 1. Differentially expressed genes in The Cancer Genome Atlas and GSE21656

Supplementary Material 26:Table 2. The gene panel derived from cisplatin resistance

Supplementary Material 27: Table 3. Mendelian randomization analysis of genes and their corresponding Genome-Wide Association Studies queue information related to the causal relationship between cisplatin resistance genomic panel and lung cancer

Supplementary Material 28:Table 4. The marker gene of CRGP high-score cell clusters (CRGPhighepi)

Supplementary Material 29:Table 5. The intersection of CRGP high-score cell clusters (CRGPhighepi) and genes filtered by Mendelian randomization for prognostic model construction (ML.genes)

Supplementary Material 30:Table 6. The intersection of CRGP high-score cell clusters (CRGPhighepi) and genes filtered by Mendelian randomization for prognostic model construction (ML.genes)

Acknowledgements
None.

Author contributions
The corresponding author is Meng Hou. The study was conceived and designed by JZL and HML. The experiments were carried out by HML, YHJ, and JZL, with administrative support from MH. Data collection was done by JZL, HML, YHJ, and JCS and data analysis and manuscript drafting were primarily handled by JZL. All authors reviewed and approved the final manuscript.

Funding
None.

Data availability
No datasets were generated or analysed during the current study.

Declarations

Ethics approval and consent to participate
Not applicable.

Consent for publication
None.

Competing interests
The authors declare no competing interests.

Received: 17 February 2025 / Accepted: 3 January 2026
Published online: 11 February 2026

References

1. Zhuo W, Zhang L, Zhu Y, Zhu B, Chen Z. Fisetin, a dietary bioflavonoid, reverses acquired cisplatin-resistance of lung adenocarcinoma cells through MAPK/Survivin/Caspase pathway. Am J Transl Res. 2015;7(10):2045–52.
2. Li W, Liu X, Zhang G, Zhang L. [Role of SOX4 on DDP resistance in Non-small cell lung cancer cell of A549]. Zhongguo Fei Ai Za Zhi. 2017;20(5):298–302.
3. Zhen J, Sun L, Ji L, Zhou S, Cui Y, Li Z. EDN1 facilitates cisplatin resistance of non-small cell lung cancer cells by regulating the TNF signaling pathway. World J Surg Oncol. 2025;23(1):71.
4. Mei J, Tian HX, Zhang XY, Chen YS, Wang LY, Zhang Z, Zhang YL, Rong DC, Zeng J, Dong M et al. Heme Oxygenase 1 (HO-1) is a drug target for reversing cisplatin resistance in non-small cell lung cancer. J Adv Res 2025. Article in Press. https://doi.org/10.1016/j.jare.2025.05.033}
5. Chatterjee D, Svoboda RA, Huisman DH, Drapkin BJ, Vieira HM, Rao C, Askew JW, Fisher KW, Lewis RE. KSR1 mediates small cell lung carcinoma tumor initiation and cisplatin resistance. Mol Cancer Res. 2025;23(6):553–66.
6. Alhaddad H, Ospina OE, Khaled ML, Ren Y, Vallebuona E, Boozo MB, et al. Spatial transcriptomics analysis identifies a tumor-promoting function of the meningeal stroma in melanoma leptomeningeal disease. Cell Rep Med. 2024;5(6):101606.
7. Cassier PA, Navaridas R, Bellina M, Rama N, Ducarouge B, Hernandez-Vargas H, et al. Netrin-1 blockade inhibits tumour growth and EMT features in endometrial cancer. Nature. 2023;620(7973):409–16.
8. Suzuki T, Sirimangkalakitti N, Baba A, Toyoshima-Nagasaki R, Enomoto Y, Saito N, et al. Characterization of the nucleotide excision repair pathway and evaluation of compounds for overcoming the cisplatin resistance of non-small cell lung cancer cell lines. Oncol Rep. 2022. https://doi.org/10.3892/or.2022.8281.
9. Wang A, Ning Z, Lu C, Gao W, Liang J, Yan Q, et al. USP22 induces cisplatin resistance in lung adenocarcinoma by regulating gammaH2AX-mediated DNA damage repair and Ku70/Bax-mediated apoptosis. Front Pharmacol. 2017;8:274.
10. Mei Y, Liu YB, Hu DL, Zhou HH. Effect of RIF1 on response of non-small-cell lung cancer patients to platinum-based chemotherapy by regulating MYC signaling pathway. Int J Biol Sci. 2018;14(13):1859–72.
11. Sarin N, Engel F, Kalayda GV, Mannewitz M, Cinatl J Jr, Rothweiler F, et al. Cisplatin resistance in non-small cell lung cancer cells is associated with an abrogation of cisplatin-induced G2/M cell cycle arrest. PLoS One. 2017;12(7):e0181081.
12. Zheng YH, Hu WJ, Chen BC, Grahn TH, Zhao YR, Bao HL, Zhu YF, Zhang QY. BCAT1, a key prognostic predictor of hepatocellular carcinoma, promotes cell proliferation and induces chemoresistance to cisplatin. Liver Int. 2016;36(12):1836–47.

13. Zhou X, Jin W, Jia H, Yan J, Zhang G. MiR-223 promotes the cisplatin resistance of human gastric cancer cells via regulating cell cycle by targeting FBXW7. J Exp Clin Cancer Res. 2015;34(1):28.
14. Fischer C, Leithner K, Wohlkoenig C, Quehenberger F, Bertsch A, Olschewski A, et al. Panobinostat reduces hypoxia-induced cisplatin resistance of non-small cell lung carcinoma cells via HIF-1alpha destabilization. Mol Cancer. 2015;14:4.
15. Ma J, Zhao Z, Wu K, Xu Z, Liu K. MCL-1 is the key target of adjuvant chemotherapy to reverse the cisplatin-resistance in NSCLC. Gene. 2016;587(2):147–54.
16. Gohr K, Hamacher A, Engelke LH, Kassack MU. Inhibition of PI3K/Akt/mTOR overcomes cisplatin resistance in the triple negative breast cancer cell line HCC38. BMC Cancer. 2017;17(1):711.
17. Hao Y, Hao S, Andersen-Nissen E, Mauck WM 3rd, Zheng S, Butler A, Lee MJ, Wilk AJ, Darby C, Zager M, et al. Integrated analysis of multimodal single-cell data. Cell. 2021;184(13):3573–87. e3529.
18. Korsunsky I, Millard N, Fan J, Slowikowski K, Zhang F, Wei K, Baglaenko Y, Brenner M, Loh PR, Raychaudhuri S. Fast, sensitive and accurate integration of single-cell data with harmony. Nat Methods. 2019;16(12):1289–96.
19. Hu C, Li T, Xu Y, Zhang X, Li F, Bai J, Chen J, Jiang W, Yang K, Ou Q, et al. CellMarker 2.0: an updated database of manually curated cell markers in human/mouse and web tools based on scRNA-seq data. Nucleic Acids Res. 2023;51(D1):D870–6.
20. Fan C, Chen F, Chen Y, Huang L, Wang M, Liu Y, et al. IrGSEA: the integration of single-cell rank-based gene set enrichment analysis. Brief Bioinform. 2024. https://doi.org/10.1093/bib/bbae243.
21. Fustero-Torre C, Jimenez-Santos MJ, Garcia-Martin S, Carretero-Puche C, Garcia-Jimeno L, Ivanchuk V, et al. Beyondcell: targeting cancer therapeutic heterogeneity in single-cell RNA-seq data. Genome Med. 2021;13(1):187.
22. Gulati GS, Sikandar SS, Wesche DJ, Manjunath A, Bharadwaj A, Berger MJ, et al. Single-cell transcriptional diversity is a hallmark of developmental potential. Science. 2020;367(6476):405–11.
23. Trapnell C, Cacchiarelli D, Grimsby J, Pokharel P, Li S, Morse M, Lennon NJ, Livak KJ, Mikkelsen TS, Rinn JL. The dynamics and regulators of cell fate decisions are revealed by pseudotemporal ordering of single cells. Nat Biotechnol. 2014;32(4):381–6.
24. Qiu X, Hill A, Packer J, Lin D, Ma YA, Trapnell C. Single-cell mrna quantification and differential analysis with census. Nat Methods. 2017;14(3):309–15.
25. Qiu X, Mao Q, Tang Y, Wang L, Chawla R, Pliner HA, Trapnell C. Reversed graph embedding resolves complex single-cell trajectories. Nat Methods. 2017;14(10):979–82.
26. Zhang Y, Liu T, Hu X, Wang M, Wang J, Zou B, et al. Cellcall: integrating paired ligand-receptor and transcription factor activities for cell-cell communication. Nucleic Acids Res. 2021;49(15):8520–34.
27. Alghamdi N, Chang W, Dang P, Lu X, Wan C, Gampala S, et al. A graph neural network model to estimate cell-wise metabolic flux using single-cell RNA-seq data. Genome Res. 2021;31(10):1867–84.
28. Cable DM, Murray E, Zou LS, Goeva A, Macosko EZ, Chen F, et al. Robust decomposition of cell type mixtures in spatial transcriptomics. Nat Biotechnol. 2022;40(4):517–26.
29. Xun Z, Ding X, Zhang Y, Zhang B, Lai S, Zou D, et al. Reconstruction of the tumor spatial microenvironment along the malignant-boundary-nonmalignant axis. Nat Commun. 2023;14(1):933.
30. Pham D, Tan X, Balderson B, Xu J, Grice LF, Yoon S, et al. Robust mapping of spatiotemporal trajectories and cell-cell interactions in healthy and diseased tissues. Nat Commun. 2023;14(1):7739.
31. Tanevski J, Flores ROR, Gabor A, Schapiro D, Saez-Rodriguez J. Explainable multiview framework for dissecting spatial relationships from highly multiplexed data. Genome Biol. 2022;23(1):97.
32. Langfelder P, Horvath S. WGCNA: an R package for weighted correlation network analysis. BMC Bioinformatics. 2008;9:559.
33. Szklarczyk D, Franceschini A, Wyder S, Forslund K, Heller D, Huerta-Cepas J, Simonovic M, Roth A, Santos A, Tsafou KP, et al. STRING v10: protein-protein interaction networks, integrated over the tree of life. Nucleic Acids Res. 2015;43(Database issue):D447–452.
34. Shannon P, Markiel A, Ozier O, Baliga NS, Wang JT, Ramage D, Amin N, Schwikowski B, Ideker T. Cytoscape: a software environment for integrated models of biomolecular interaction networks. Genome Res. 2003;13(11):2498–504.
35. Fawzy MA, Beshay ON, Bekhit AA, Abdel-Hafez SMN, Batiha GE, Bin Jardan YA, et al. Nephroprotective effect of AT-MSCs against cisplatin-induced EMT is improved by Azilsartan via attenuating oxidative stress and TGF-beta/Smad signaling. Biomed Pharmacother. 2023;158:114097.
36. Cho HJ, Kim IK, Park SM, Baek KE, Nam IK, Park SH, et al. VEGF-C mediates RhoGDI2-induced gastric cancer cell metastasis and cisplatin resistance. Int J Cancer. 2014;135(7):1553–63.
37. Uygur B, Leikina E, Melikov K, Villasmil R, Verma SK, Vary CPH, et al. Interactions with muscle cells boost fusion, stemness, and drug resistance of prostate cancer cells. Mol Cancer Res. 2019;17(3):806–20.
38. Wang Z, Chen W, Zuo L, Xu M, Wu Y, Huang J, et al. The fibrillin-1/VEGFR2/STAT2 signaling axis promotes chemoresistance via modulating glycolysis and angiogenesis in ovarian cancer organoids and cells. Cancer Commun (Lond). 2022;42(3):245–65.
39. Li Y, Xiao S, Dan L, Xue M. P16(INK4A) is required for cisplatin resistance in cervical carcinoma SiHa cells. Oncol Lett. 2015;9(3):1104–8.
40. Zhao X, He R, Liu Y, Wu Y, Kang L. Upregulated single-stranded DNA-binding protein 1 induces cell chemoresistance to cisplatin in lung cancer cell lines. Mol Cell Biochem. 2017;431(1–2):21–7.
41. Huang RS, Zheng YL, Zhao J, Chun X. MicroRNA-381 suppresses the growth and increases cisplatin sensitivity in non-small cell lung cancer cells through inhibition of nuclear factor-kappaB signaling. Biomed Pharmacother. 2018;98:538–44.
42. Zheng SZ, Sun P, Wang JP, Liu Y, Gong W, Liu J. MiR-34a overexpression enhances the inhibitory effect of doxorubicin on HepG2 cells. World J Gastroenterol. 2019;25(22):2752–62.
43. Qu W, Huang W, Yang F, Ju H, Zhu G. Long noncoding RNA LINC00461 mediates cisplatin resistance of rectal cancer via miR-593-5p/CCND1 axis. Biomed Pharmacother. 2020;124:109740.
44. Kim SH, Ho JN, Jin H, Lee SC, Lee SE, Hong SK, Lee JW, Lee ES, Byun SS. Upregulated expression of BCL2, MCM7, and CCNE1 indicate cisplatin-resistance in the set of two human bladder cancer cell lines: T24 cisplatin sensitive and T24R2 cisplatin resistant bladder cancer cell lines. Investig Clin Urol. 2016;57(1):63–72.
45. Ma J, Li J, Yao X, Lin S, Gu Y, Xu J, et al. FIGNL1 is overexpressed in small cell lung cancer patients and enhances NCI-H446 cell resistance to cisplatin and etoposide. Oncol Rep. 2017;37(4):1935–42.
46. Pan H, Li J, Rankin GO, Rojanasakul Y, Tu Y, Chen YC. Synergistic effect of black tea polyphenol, theaflavin-3,3′-digallate with cisplatin against cisplatin resistant human ovarian cancer cells. J Funct Foods. 2018;46:1–11.
47. Zhao ZM, Yost SE, Hutchinson KE, Li SM, Yuan YC, Noorbakhsh J, et al. CCNE1 amplification is associated with poor prognosis in patients with triple negative breast cancer. BMC Cancer. 2019;19(1):96.
48. Xiong GB, Yang G, Feng MY, Zhao FY, Zheng LF, Zhang TP, et al. [The long coding RNA GSTM3TV2 acts an oncogene to promote chemoresistance in pancreatic cancer]. Zhonghua Wai Ke Za Zhi. 2019;57(9):691–7.
49. Ji LY, Wei M, Liu YY, Di ZL, Li SZ. MiR-497/MIR497HG inhibits glioma cell proliferation by targeting CCNE1 and the miR-588/TUSC1 axis. Oncol Rep. 2021. https://doi.org/10.3892/or.2021.8206.
50. Wei X, Shi J, Lin Q, Ma X, Pang Y, Mao H, et al. Targeting ACLY attenuates tumor growth and acquired cisplatin resistance in ovarian cancer by inhibiting the PI3K-AKT pathway and activating the AMPK-ROS pathway. Front Oncol. 2021;11:642229.
51. Shen D, Wang Y, Niu H, Liu C. Gambogenic acid exerts anticancer effects in cisplatin–resistant non–small cell lung cancer cells. Mol Med Rep. 2020;21(3):1267–75.
52. Hong S, Li X, Zhao Y, Yang Q, Kong B. 53BP1 inhibits the migration and regulates the chemotherapy resistance of ovarian cancer cells. Oncol Lett. 2018;15(6):9917–22.
53. Santana-Rivera Y, Rabelo-Fernandez RJ, Quinones-Diaz BI, Grafals-Ruiz N, Santiago-Sanchez G, Lozada-Delgado EL, Echevarria-Vargas IM, Apiz J, Soto D, Rosado A, et al. Reduced expression of enolase-1 correlates with high intracellular glucose levels and increased senescence in cisplatin-resistant ovarian cancer cells. Am J Transl Res. 2020;12(4):1275–92.
54. Zhang X, Huang J, You F, Li W, Zou Z. Prognostic and clinicopathological significance of LOXL2 in cancers: a systematic review and meta-analysis. J Cell Physiol. 2019;234(11):21369–79.

Publisher's note